Ore Geology Reviews 88 (2017) 534–549

Contents lists available at ScienceDirect

Ore Geology Reviews

journal homepage: www.elsevier.com/locate/oregeorev

A hydrothermal origin for the large Xinqiao Cu-S-Fe deposit, Eastern China: Evidence from sulfide geochemistry and sulfur isotopes

Yu Zhang [a,b,c], Yong-jun Shao [b,c,*], Hua-yong Chen [a,d], Zhong-fa Liu [b,c], Deng-feng Li [a]

[a] Key Laboratory of Mineralogy and Metallogeny, Guangzhou Institute of Geochemistry, Chinese Academy of Sciences, Guangzhou 510640, China
[b] Key Laboratory of Metallogenic Prediction of Nonferrous Metals and Geological Environment Monitor (Central South University), Ministry of Education, Changsha 410083, China
[c] School of Geosciences and Info-Physics, Central South University, Changsha 410083, China
[d] Guangdong Provincial Key Laboratory of Mineral Physics and Materials, Guangzhou 510640, China

ARTICLE INFO

Article history:
Received 21 January 2016
Received in revised form 1 August 2016
Accepted 3 August 2016
Available online 6 August 2016

Keywords:
Xinqiao Cu-S-Fe deposit
Middle-Lower Yangtze River Valley metallogenic belt (MLYB)
Stratiform and skarn mineralization
Pyrite geochemistry and isotopes
Yanshanian magmatism-mineralization

ABSTRACT

The Xinqiao Cu-S-Fe deposit in the Tongling ore district, Middle-Lower Yangtze River Valley Metallogenic Belt (MLYB; Eastern China), is located along the northern margin of the Yangtze Craton. The stratiform- and skarn-type Xinqiao mineralization comprises five stages, namely the early skarn (Stage I, garnet and diopside), late skarn (Stage II, epidote-dominated), iron oxides (Stage III, hematite and magnetite), colloform pyrite (Stage IV) and quartz-sulfides (Stage V). There are three pyrite types at Xinqiao, i.e., colloform (Py1; Stage IV), fine-grained (Py2, from Py1 recrystallization; Stage V) and coarse-grained (Py3; Stage V) pyrites.

Scanning Electron Microscope (SEM) imagery for Py1 reveals that they are cubic microcrystalline pyrite aggregates, and the EDS and XRD data indicate that some Py1 contain minor siderite impurities. Electron Microprobe Analysis (EMPA) and LA-ICP-MS geochemical data demonstrate that the three pyrite types have relatively high Fe/S ratios and distinctly high Mn, Cu and As concentrations. Compared to Py2 and Py3, Py1 has higher Pb, Bi and Ag, but lower Co, Ni, Se, Cd, Te and Au. Ratios of Fe/S (0.837 to 0.906), Se/Te (2.39 to 14.50) and Co/Ni (0.67 to 4.67) of the Xinqiao pyrites resemble typical hydrothermal pyrites. $\delta^{34}S_{CDT}$ of Py1 (−0.6‰ to 2.7‰, average 0.58‰), Py2 (1.8‰ to 2.5‰, average 2.1‰) and Py3 (1.9‰ to 4.4‰, average 3.5‰) are close to those of the Xinqiao skarn-type orebodies (1.3‰ to 4.1‰), but distinct from those of the Upper Carboniferous Huanglong Formation limestone (−9.5‰ to −15.4‰), suggesting that the three pyrite types (especially Py1) were genetically linked to the Yanshanian (Jurassic-Cretaceous) magmatic-hydrothermal events, with Py1 probably reflecting rapid crystallization during fluid mixing. We interpret that the Xinqiao stratiform mineralization may have been associated with the Jitou quartz diorite stock, as may be the case also for the skarn-type mineralization hosted in the contact between the Yanshanian Jitou stock and the Lower Permian Qixia Formation limestone. Overall, the Xinqiao Cu-S-Fe mineralization may have been generated by the Jurassic-Cretaceous tectono-thermal event in Eastern China.

1. Introduction

The Tongling ore district is an important part of the Middle-Lower Yangtze River Valley metallogenic belt (hereinafter referred to as MLYB; Wang et al., 2015) situated along the northern margin of the Yangtze Craton (Eastern China; Fig. 1), and is featured by the widespread Yanshanian (Jurassic-Cretaceous) granitoids and their associated skarn deposits, such as the Tongguanshan, Fenghuangshan and Shizishan Cu deposits (Mao et al., 2009). The presence of large stratiform orebodies at the Xinqiao Cu-S-Fe and Dongguashan Cu-Au deposits has added extra complexities to the regional metallogenesis.

The Xinqiao Cu-S-Fe deposit is one of the largest deposits in the Tongling ore district (0.5 Mt Cu @ 0.71%, 75.5 Mt sulfur @ 29.3%, 24.9 Mt Fe @ 46%, 11.2 t Au @ 4.7 g/t and 248.4 t Ag @ 248.4 g/t; Xu and Zhou, 2001). The Xinqiao stratiform mineralization has been controversial over the past forty years. The #803 Geological Brigade had conducted systematic exploration at Xinqiao between 1963 and 1971, and considered that the stratiform mineralization was resulted from hydrothermal replacement related to the Jurassic-Cretaceous magmatism, yet no age data were available to support this (803 Geological Brigade of East China Metallurgical and Geological Exploration, 1971).

Dacitic lava and volcaniclastic rocks at the bottom of the ore-hosting strata were considered to be related to the Hercynian (Late Paleozoic) submarine exhalation mineralization (Fu et al., 1977; Xu and Zhu,

* Corresponding author at: Key Laboratory of Metallogenic Prediction of Nonferrous Metals and Geological Environment Monitor (Central South University), Ministry of Education, Changsha 410083, China.
E-mail address: shaoyongjun@126.com (Y. Shao).

http://dx.doi.org/10.1016/j.oregeorev.2016.08.002
0169-1368/

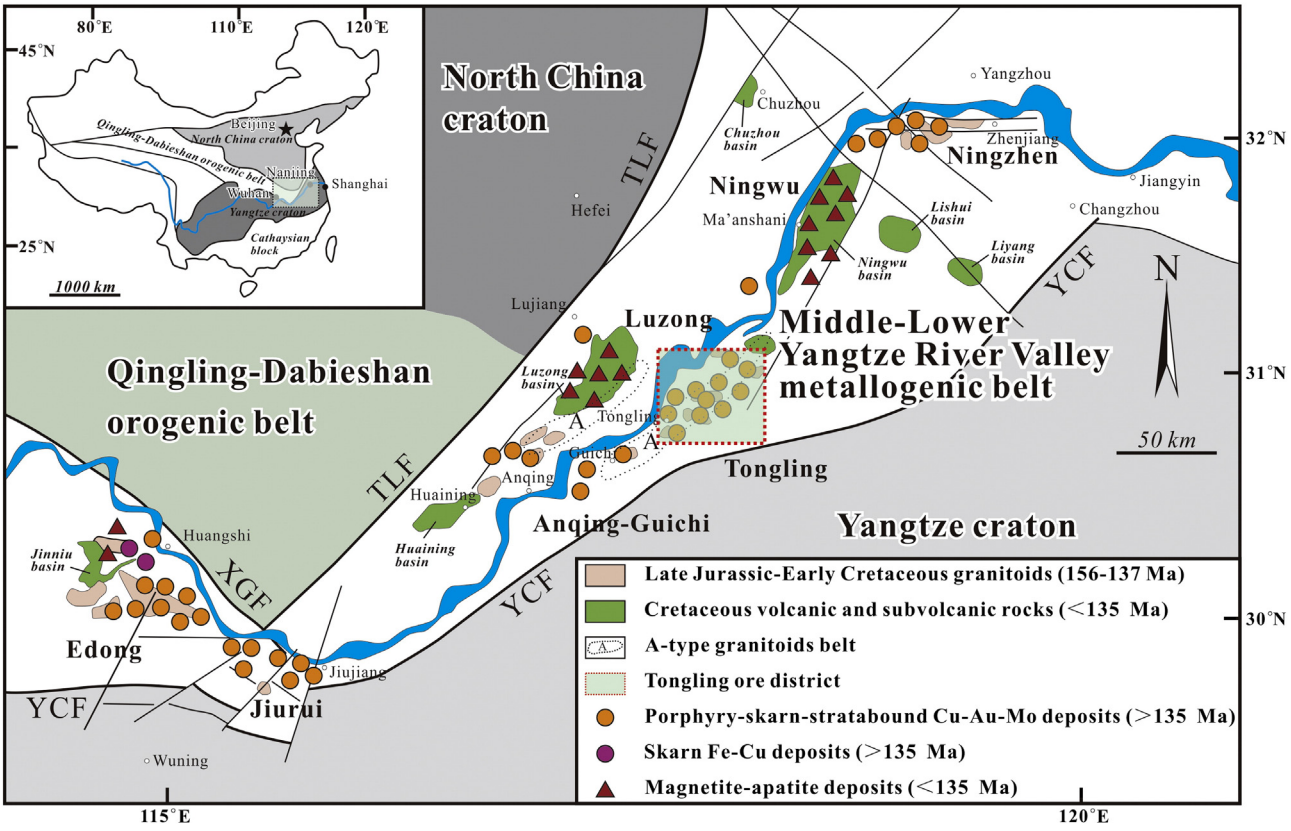

Fig. 1. Location of Tongling ore district in the MLYB (after Mao et al., 2011). TLF: Tancheng–Lujiang fault; XGF: Xiangfan–Guangji fault; YCF: Yangxing–Changzhou fault.

1978). The newly-identified colloform pyrite in the stratiform orebody has typical syn-depositional texture, and the stockwork mineralization at the stratiform orebody footwall mimics the dual structure of typical sedimentary exhalative (SEDEX) deposits. These two features were interpreted to support the Late Paleozoic submarine exhalation mineralization hypothesis (Gu and Xu, 1986; Gu et al., 2000; Xu and Zhou, 2001; Xu et al., 2004). Pyrites from the footwall stockwork mineralization (Guo et al., 2011) were Re-Os dated to be late Carboniferous (319 ± 13 Ma).

Based on the metallogenesis of the Tongling ore district and local ore deposit geology, Chang and Liu (1983); Yang and Wang (1985); Chang et al. (1991); Zhai et al. (1992); Meng (1994, 1996); Pan and Done (1999) alternatively suggested that the Xinqiao mineralization was related to the Jurassic-Cretaceous tectono-thermal event in Eastern China, and that the stratiform orebody may have formed by hydrothermal alteration along the detachment contact between the Upper Devonian Wutong Formation quartz sandstone and the Upper Carboniferous Huanglong Formation limestone. Mao et al. (2009, 2011) supported this view because the parallel ore-hosting unconformity between the Wutong and Huanglong formations sediments is much shallower than what SEDEX typically occurs and the major alteration mineral assemblage (quartz + pyrite) of the footwall stockwork mineralization is distinct from that of the sedimentary exhalative deposit (anhydrite and barite; Sangster, 1990). The H-O isotope data of the ore-bearing quartz (Liu, 2002), and Re-Os isochron (126 ± 11 Ma; Xie et al., 2009) ages of the pyrites from the stratiform orebody are coeval with the Jurassic-Cretaceous magmatic-hydrothermal activities, but this does not preclude the possibility that the orebodies were formed via a Jurassic-Cretaceous mineralization overprinting on the Late Paleozoic submarine exhalation mineralization (Yang et al., 1982; Liu, 1991; Xie et al., 1995; Tang et al., 1998; Zhou et al., 2010). Moreover, Fe isotope (δ^{57}Fe: −1.22‰ to 0.15‰) of colloform pyrite mineral separates from the Xinqiao stratiform orebody indicates a magmatic-hydrothermal origin rather than a syngenetic sedimentary origin (Wang et al., 2011, 2013), and the colloform pyrite was thought to be the result of rapid crystallization of magmatic-hydrothermal fluids (Meng, 1994, 1996; Ren and Liu, 2006). However, optical microscopy observations show that almost all the colloform pyrite grains contain some crystalline pyrites, and hence the Fe isotope result of colloform pyrite mineral separates possibly reflects a mixture of both.

Pyrite trace elements geochemistry provides useful information for determining the ore-forming fluid sources and evolution (Cook et al., 2009; Maslennikov et al., 2009; Large et al., 2009; Sung et al., 2009; Thomas et al., 2011; Zhao et al., 2011; Zhang et al., 2014). Zhou et al. (2010) first conducted a laser ablation inductively coupled plasma mass spectrometry (LA-ICP-MS) analysis on the Xinqiao pyrites, and argued that the colloform pyrite may have been sedimentary- or submarine exhalation-derived, and that the metals (e.g., Cu, Pb, Zn, Au and Ag) may have come mostly from the Jurassic-Cretaceous magmatic-hydrothermal system related to the Jitou stock. However, the limited dataset (three analyses) of colloform pyrites does not allow undisputed conclusions. Xiao et al. (2016) carried out field emission scanning electron microscopy (FE-SEM) and LA-ICP-MS analyses on the Xinqiao pyrites and reached the same conclusion as Zhou et al. (2010), but the Co/Ni values (range widely from 0.01 to 14.67, average 1.57) reported for the colloform pyrites are inconsistent with that for a sedimentary origin.

This study carries out in situ analyses of major and trace elements and sulfur isotope for the pyrite from the Xinqiao stratiform orebody by using the Electron Probe Microanalyzer (EPMA), LA-ICP-MS and the Sensitive High Resolution Ion Microprobe (SHRIMP), respectively, based on detailed field investigation and mineralogical study (especially SEM/EDS and XRD analyses for the colloform pyrite). We aimed to characterize the geochemistry of the various pyrite types and elucidate their origin, in order to better constrain the large-scale Cu-S-Fe metallogeny at Xinqiao.

2. Geological setting

2.1. Regional geology

The Tongling ore district is an important part of MLYB, containing five orefields (from east to west), namely Tongguanshan, Shizishan, Xinqiao, Fenghuangshan and Shatanjiao. Sedimentary rocks exposed in the area have ages spanning from the Silurian to the Cretaceous, among which the Carboniferous Huanglong and Chuanshan formations limestone and the Triassic Nanlinghu Formation limestone are important ore-hosting strata. Structurally, the region contains mainly NE-trending folds and NNE- and NW-trending faults which control the intrusion emplacement. Igneous rocks are widely distributed in the region, and are dominated by Late Jurassic-Early Cretaceous (ca. 156 to 137 Ma) high-K calc-alkaline granitoids (e.g., diorite, quartz diorite and granodiorite) (Mao et al., 2011).

2.2. Ore deposit geology

Sedimentary rocks in the Xinqiao mining area consist of the Middle-Upper Silurian sandstone and siltstone (the Maoshan and Fentou formations) and Lower Triassic limestone (the Yinkeng Formation). Major structures at Xinqiao are the NE-oriented Dachengshan anticline and the NNE-oriented Shenchong syncline (Fig. 2). The Jitou stock occurs in the core of the Shenchong syncline, and is composed of quartz diorite at the center and diorite porphyry along the edges. The Jitou stock has a SHRIMP zircon U-Pb age of 140.4 ± 2.2 Ma (Wang et al., 2004a,b).

The two major mineralization types at Xinqiao include: An economically significant stratiform mineralization (accounting for 90% of the Cu, S and Fe reserves) is constrained in the detachment zone between the Upper Devonian Wutong Formation quartz sandstone and the Upper Carboniferous Huanglong Formation limestone; and an economically less important skarn-type mineralization hosted in the contact between the Yanshanian quartz diorite and the Lower Permian Qixia Formation limestone (Fig. 3).

The Middle and Upper Carboniferous Huanglong and Chuanshan formations are mainly composed of limestone, which were extensively replaced by the stratiform ores and became the main ore-hosting strata. The Upper Devonian Wutong Formation, dominated by quartz sandstone, acts as the footwall of the stratiform orebody, in which there are pyrite-bearing quartz stockwork (Fig. 4a). The Lower Permian Qixia Formation overlies the stratiform orebody, and is composed of limestone and chert. The stratiform orebody is 2560 m long, 1810 m wide and on average 21 m thick. The orebody is dipping to the northwest, parallel with the Upper Devonian Wutong Formation and the Upper Carboniferous Huanglong Formation (Fig. 3), and is in abrupt contact with the Wutong Formation quartz sandstone (Fig. 4b). Field geologic and petrographic observations indicate that ore minerals in the stratiform orebody are dominated by magnetite, chalcopyrite, pyrrhotite and hematite, with gangue minerals including garnet, diopside, epidote, chlorite, quartz and calcite. Zonation of metallic mineral

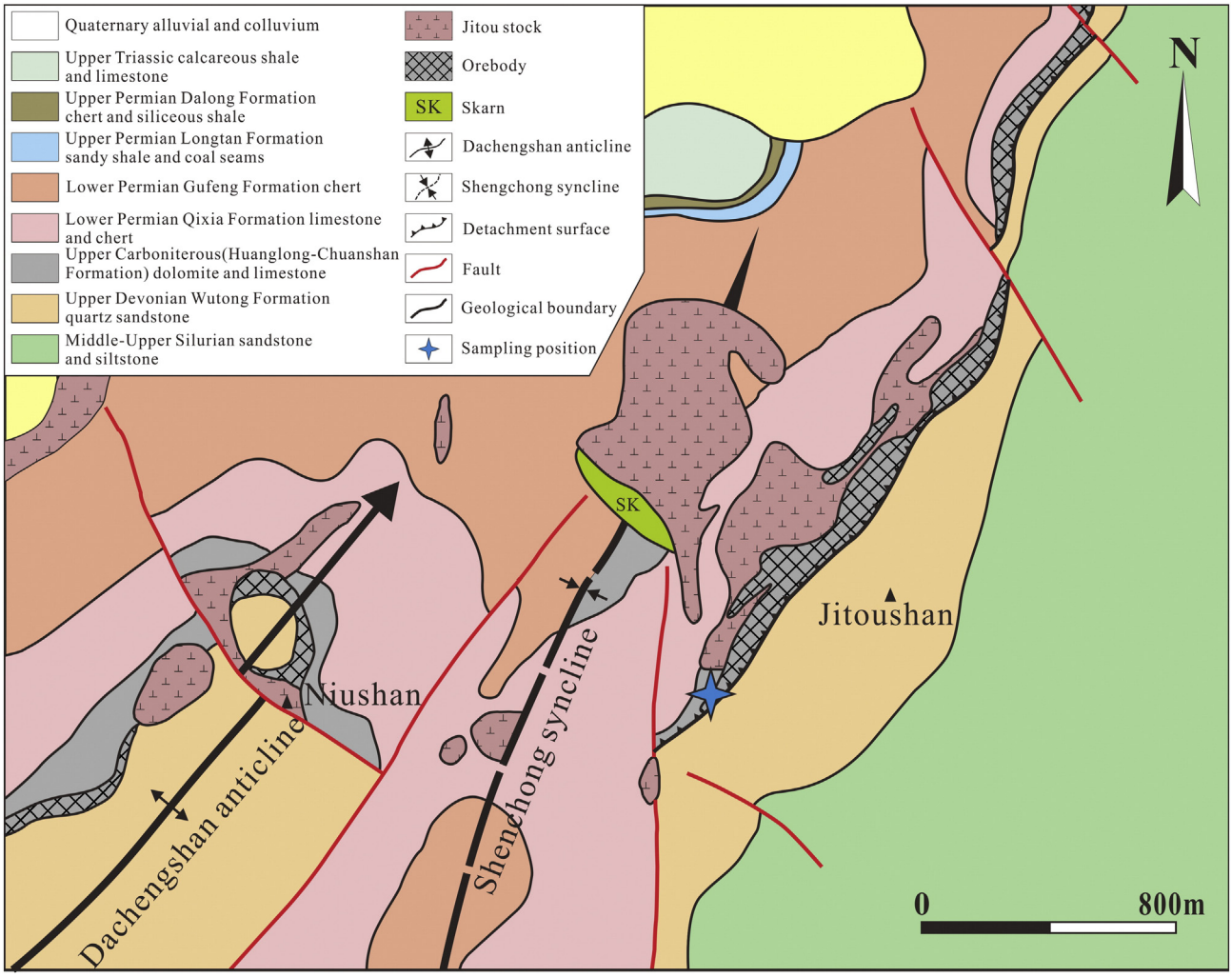

Fig. 2. Geological map of Xinqiao Cu-S-Fe deposit (after Tang et al., 1998).

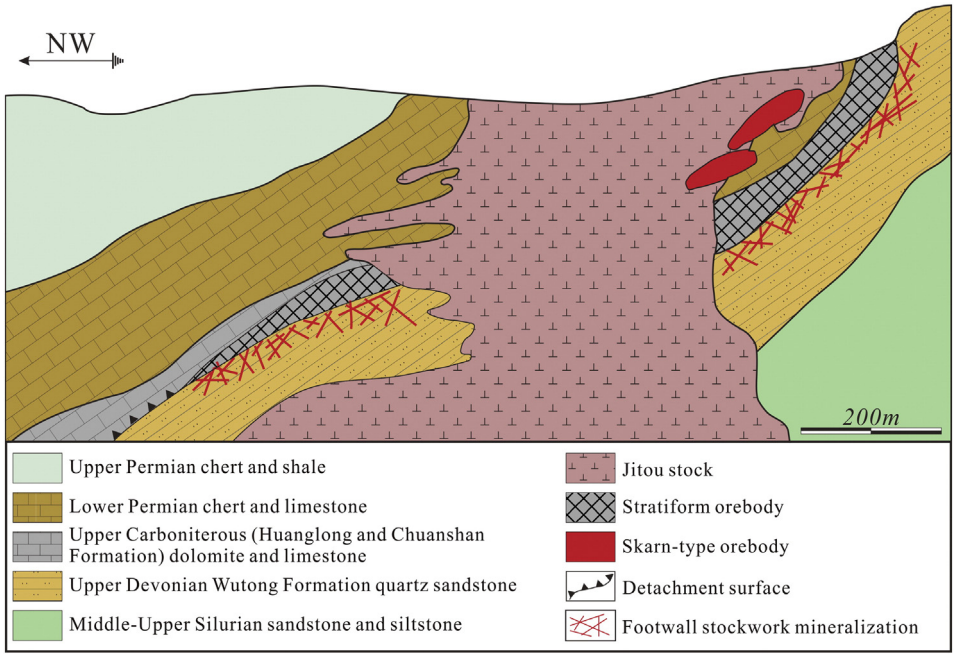

Fig. 3. Representative cross-section of the Xinqiao Cu-S-Fe deposit (after Zang et al., 2004).

assemblages occurs in the stratiform orebody away from the Jitou stock, from magnetite + pyrite, through chalcopyrite + pyrite to pyrite. In addition, the colloform pyrite is the mineral with typical colloform or concentric ring textures in the southwestern end of the stratiform orebody (Xie et al., 2014; Xiao et al., 2016).

The skarn-type orebodies account for 10% of the metal reserves at Xinqiao, and are developed along the contact between the Jitou stock and the Lower Permian Qixia Formation limestone. Both the endoskarn and exoskarn are garnet skarn, consisting predominately of garnet, wollastonite and subordinate pyroxene (Wang et al., 2011).

Detailed field investigation indicates that the wall rock alteration styles of the stratiform orebody mainly include garnet, diopside, epidote, sericite, quartz, chlorite and kaolinite alterations. Only the alteration of chert was identified in the Wutong Formation quartz sandstone, footwall of the stratiform orebody (Fig. 4a).

3. Paragenetic sequences of mineralization and alteration

Based on the mineral assemblages and textural relationships, mineralization at Xinqiao can be subdivided into five stages (Fig. 5), namely the early skarn (Stage I), late skarn (Stage II), iron oxides (Stage III), colloform pyrite (Stage IV) and the quartz-sulfide (Stage V) stages. Stage III can be further divided into the hematite (Stage IIIA) and magnetite (Stage IIIB) sub-stages, and Stage V can be further divided into the quartz-pyrite (Stage VA) and quartz-chalcopyrite (Stage VB) sub-stages.

Stage I is dominated by abundant garnet and diopside coexisting with trace wollastonite (Xie, 2012). Garnet is euhedral or anhedral granular texture (Fig. 6a-c). Diopside is mainly subhedral granular or allotriomorphic prismatic texture (Fig. 6a). Locally, garnet and diopside were replaced by epidote and corroded by magnetite (Fig. 6a), which indicates that epidote and magnetite were formed later than garnet and diopside.

Stage II is characterized by abundant epidote coexisting with trace tremolite (Xie, 2012), most of which contains allotriomorphic texture and occurs within the Stage I garnet grains (Fig. 6b). Some epidotes replaced garnet and diopside pseudomorphs (Fig. 6a). Locally, epidote was replaced by magnetite (Fig. 6b) and corroded Stage I garnet grains (Fig. 6c), indicating that epidote formed after garnet but before magnetite.

Stage IIIA is mainly composed of radial or needle-like hematite, whose pseudomorphs were usually filled in by later magnetite (Fig.

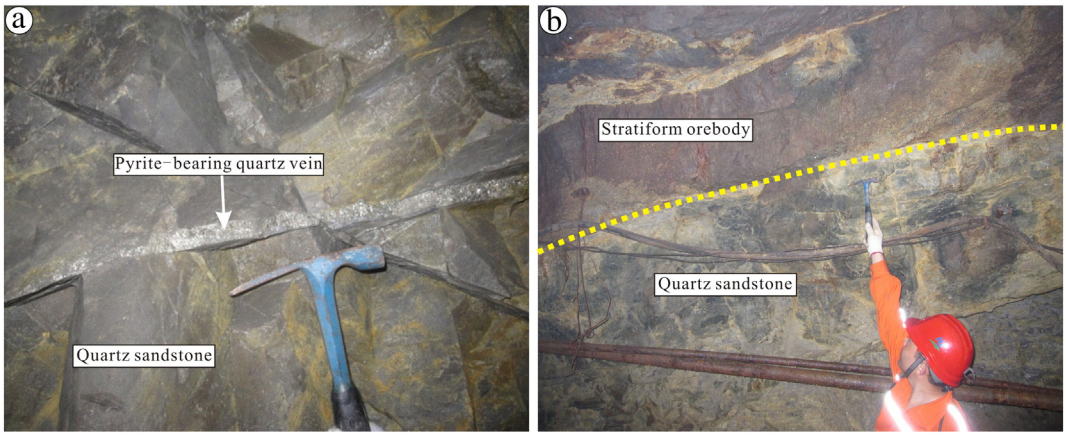

Fig. 4. (a) Pyrite-bearing quartz vein in the Wutong Formation quartz sandstone and (b) the abrupt contact interface between the Xinqiao stratiform orebody and the Wutong Formation quartz sandstone.

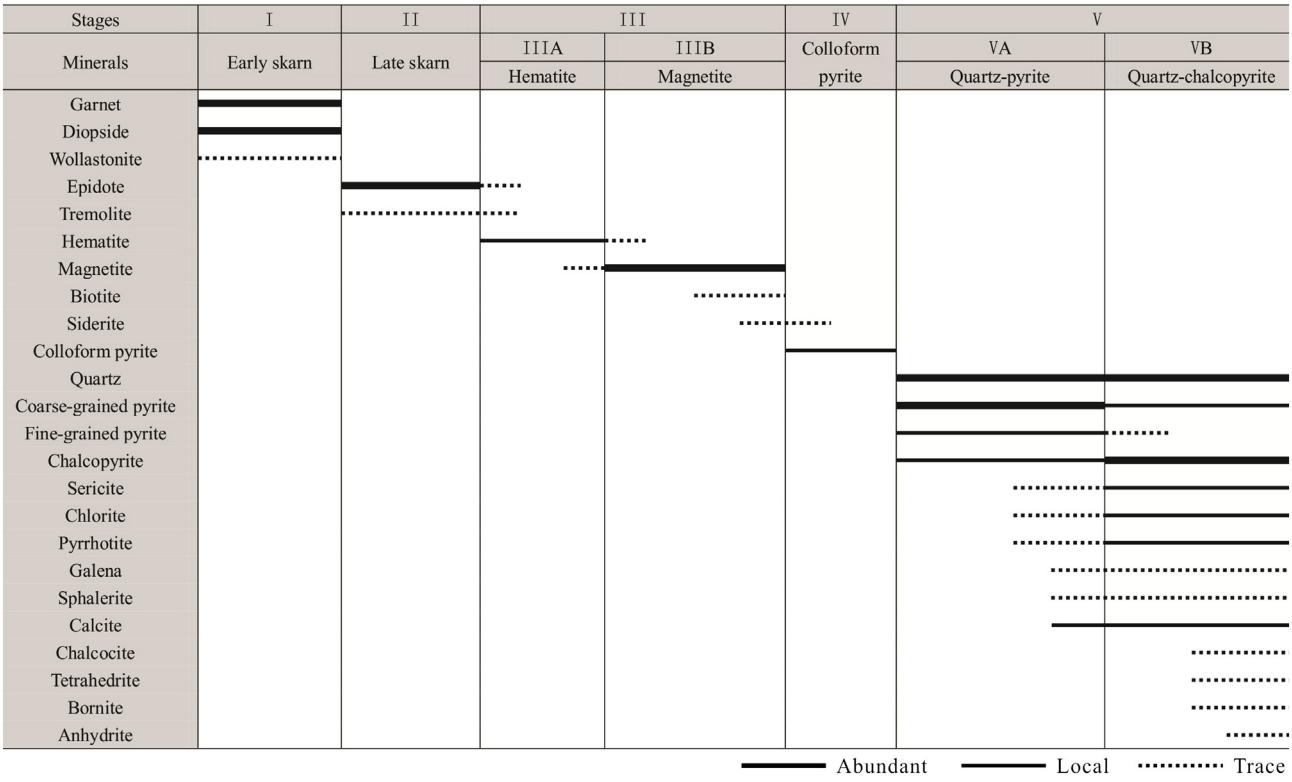

Fig. 5. Mineral paragenesis of the Xinqiao deposit.

6d–e). *Stage IIIB* (magnetite) is the most important Fe mineralization stage, in which massive magnetite was cut by Stage V pyrite veins (Fig. 6f). Hematite-bearing magnetite grains were locally replaced by late pyrite along the grain boundaries (Fig. 6g).

Stage IV is characterized by colloform pyrite (Py1), hand-specimen of which is light grey and massive without metallic luster (Fig. 6h). A single Py1 grain is usually 0.5 mm to 0.7 mm in diameter, and shows typical colloform or concentric ring textures (Fig. 6i–j). The majority of Py1 has experienced recrystallization and transformed into Stage VA fine-grained pyrite (Py2), which commonly has metasomatic relict and blastoaplitic texture (Fig. 6i). Py1 grains are locally cut by the Stage V coarse-grained pyrite (Py3) veins (Fig. 6j). In addition, Py1 and coarse-grained Py3 were also found to cement Stage IIIB massive magnetite (Fig. 6k), which indicates that the colloform Py1 was formed after magnetite.

Stage VA is characterized by abundant Py3 coexisting with abundant quartz and minor Py2 (Fig. 6i) and chalcopyrite (Fig. 6l). Py3 locally replaces magnetite (Fig. 6m). *Stage VB* is the main Cu mineralization stage and contains abundant quartz, calcite, chalcopyrite and pyrite, together with minor pyrrhotite, galena, sphalerite, sericite and chlorite. Guo et al. (2011) and Xie (2012) reported that trace Cu-bearing sulfides (chalcocite, tetrahedrite, bornite) and anhydrite formed at this sub-stage. Chalcopyrite mainly occurs as allotriomorphic texture, in quartz-bearing veins (Fig. 6n) and stockworks (Fig. 6o). Quartz-bearing chalcopyrite veins locally crosscut Stage VA Py2 (Fig. 6n), and chalcopyrite stockwork locally crosscut Stage VA Py3 (Fig. 6o). Pyrrhotite mainly occurs as allotriomorphic texture, which locally replaces Stage VA Py3 (Fig. 6p). Sphalerite locally occurs as veins together with pyrite, chalcopyrite and quartz (Fig. 6q). Stage VB Py3 locally replaces Stage VA Py2 (Fig. 6i).

4. Sampling and analytical methods

Three pyrite samples were collected from the top of a stratiform orebody in the southeast part of the 60 m platform at the Xinqiao open pit (XQ11-7, Fig. 2) and a stratiform orebody in the E16 stope at an underground depth of −270 m (XQ43-4 and XQ43-9). These samples usually contain all the three pyrite types and show massive structure (Fig. 6h–i). It is difficult to keep the Py1 sample for long under normal circumstances because it is very easily oxidized, which leads to a change from massive texture to powder and the formation of light green, needle-like and transparent minerals (Fig. 6r).

Sample preparation includes mainly laser mount preparation and petrographic microscopy at the Key Laboratory of Metallogenic Prediction of Nonferrous Metals and Geological Environment Monitor (Central South University), Changsha, China.

Morphology observation and EDS analysis for Py1 were performed using a field emission scanning electron microscope (Sirion200, FEI, American) in combination with Energy Dispersive Spectroscopy (EDS) (GENESIS 60S, FEI, American) at the Key Laboratory of Nonferrous Metal Materials Science and Engineering (Central South University). XRD analysis for Py1 was performed using a TTR3 X-ray diffraction (XRD) (Shimadzu, Japan) at the Key Laboratory of Metallogenic Prediction of Nonferrous Metals and Geological Environment Monitor (Central South University). Analytical conditions include 50 kv (voltage), 200 mA (electric current) and 8° per minute (scanning speed).

The electron microprobe (EPMA) analysis for sample was carried out in the School of Geosciences and Info-Physics of the Central South University, using an 1720 EPMA from the Shimadzu Corporation, Japan. Analytical parameters include 15 kv (acc. Voltage), 2.0×10^{-8} A (probe current) and 1 μm (spot size), and with 0.01% detection limit. Elements analyzed include Fe, S, As, Co, Ni, Sb, Ag and Au.

Subsequently, LA-ICP-MS analysis was conducted at the Center for Geo-Environmental Science, Akita University, Japan, using an Agilent 7500i quadrupole mass spectrometer and New Wave Research 5906 laser ablation system. Helium is the carrier gas of the ablated materials during the experiment, and analytical parameters are 45 μm for spot size, 6 Hz for frequency and 6.5 J/cm^2 for laser energy. Analysis time of one spot is 90 s, including 30 s of background (pre-ablation), 30 s for standards and 30 s for the samples.

In addition, samples were analyzed for $\delta^{34}S_{CDT}$ using SHRIMP-SI at the Australian National University. The methodology was described in detail

by Gregory et al. (2014). Prior to the analysis, the mounts holding the samples were coated in 0.01 μm of gold to dissipate the charge build up during analysis, and to stabilize the −10 kV sample potential, so that secondary ions emitted from the surface have a uniform potential. The source chamber pressure was maintained at 10^{-6} Pa. Primary Cs^{+} ions were produced and accelerated to +5 kV in the Kimball Physics IGS-4

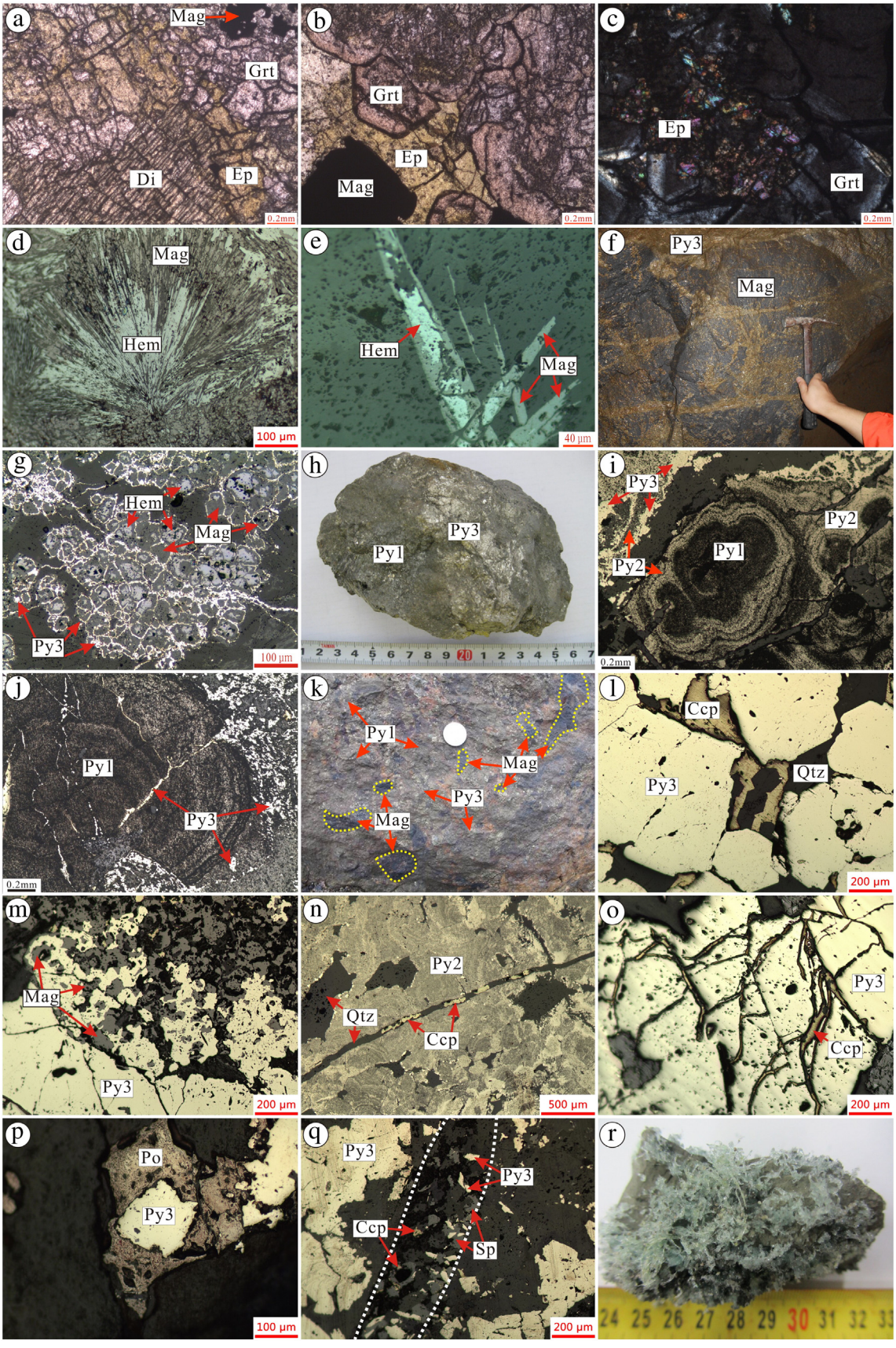

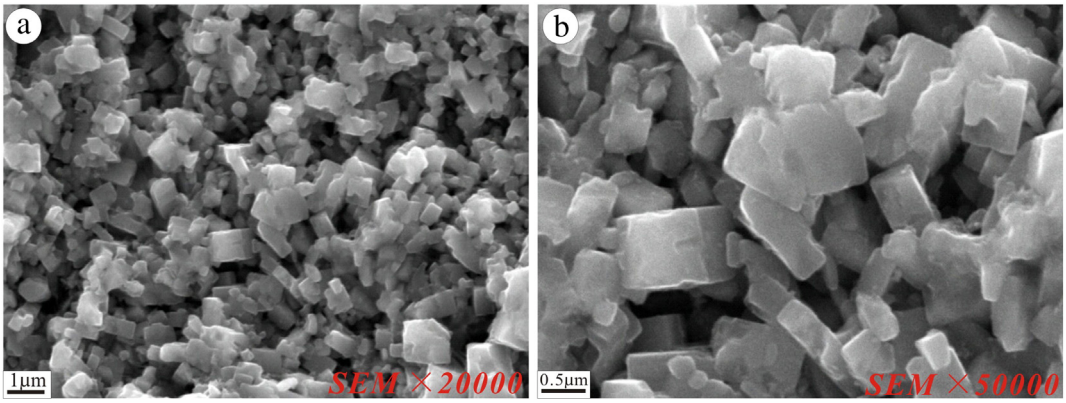

Fig. 7. SEM photographs of colloform pyrites, showing the colloform pyrite being an aggregate of cubic microcrystalline pyrites. (a) 20 k× magnification; (b) 50 k× magnification.

ion gun while the sample surface was held at −10 kV, making the impact energy 15 keV. The primary ion beam was focused to 25 μm. The area surrounding the analysis spot was pre-ablated, and sputtered for 120 s to ensure secondary ion beam stability prior to data acquisition. The analysis consists of 10 cycles of 10 s data acquisition intervals. The different sulfur isotopes were measured using Faraday cups (Ireland et al., 2014). Ruttan pyrite was used as the primary standard, and approximately two analyses of the standard were conducted for every seven analyses.

5. Results

5.1. SEM, EDS and XRD

Py1 SEM imaging under 2×10^4 to 5×10^4 times magnification shows that a single colloform pyrite grain comprises an aggregate of cubic microcrystalline pyrites of different sizes (<1 μm, Figs. 7a–b), which are different from framboidal pyrite composed of similarly-sized microcrystalline pyrites (Rickard, 1970). EDS analysis shows that most Py1 contains only Fe and sulfur (Fig. 8a), and some contain also carbon and oxygen (Fig. 8b). This is well explained by the XRD analytical data, which show that most Py1 aggregates contain only pyrites (Fig. 9a), whereas some contain also minor siderites impurities (Fig. 9b).

XRD analysis for oxidized materials (light green, needle-like and transparent, Fig. 6r) were also conducted on Py1, which shows that they are rozenite ($FeSO_4 \cdot 4H_2O$) and melanterite ($FeSO_4 \cdot 7H_2O$) (Fig. 10).

5.2. EPMA

A total of 29 EPMA spot analyses were completed on pyrites, including seven spots on Py1, ten spots on Py2 and 12 spots on Py3. The results (Table 1) indicate that Py1, Py2 and Py3 have sulfur concentrations of 51.79–53.17 wt.% (average 52.59 wt.%), 52.25–53.47 wt.% (average 52.95 wt.%), 52.22–54.30 wt.% (average 53.08 wt.%), respectively, and Fe concentrations vary from 46.51–47.68 wt.% (average 46.98 wt.%), 46.46–47.79 wt.% (average 47.21 wt.%) to 45.44–47.82 wt.% (average 46.97 wt.%), respectively. The As, Co, Ni, Sb, Ag and Au concentrations of the three pyrite types are 0.01–1.15 wt.%, 0.02–0.57 wt.%, 0.01–0.04 wt.%, 0.01–0.04 wt.%, 0.01–0.06 wt.% and 0.01–0.19 wt.%, respectively.

5.3. LA-ICP-MS

A total of 34 LA-ICP-MS spot analyses were completed on pyrites, including 13 spots on Py1, seven spots on Py2 and 14 spots on Py3. Trace elements contents for the three pyrite types are shown in Table 2 and Fig. 11.

In general, concentrations for most trace elements in Py2 and Py3 vary considerably, and Py1 contains a narrower range of Co, Ni, Pb, Bi, Cu, As, Ag, Sb, Tl, Te and Se, higher Pb, Bi and Ag, and lower Co, Ni, Se, Cd, Te and Au.

The Mn, Cu and As contents in Py1, Py2 and Py3 are distinctly higher than other trace elements, and the averages can reach hundreds of ppm (Table 3). Cobalt and Ni are two important and common trace elements in pyrite worldwide. Py2 and Py3 have the similar Co and Ni concentrations, and are both higher than those of Py1 (Table 3).

5.4. SHRIMP

A total of 30 SHRIMP spot analyses were completed on pyrites, including 21 spots on Py1, four spots on Py2 and five spots on Py3. In-situ sulfur isotope data (Table 4; Figs. 12–13) show that $\delta^{34}S_{CDT}$ of Py1, Py2 and Py3 are −4.6–2.7‰ (average 0.6‰), 1.8–2.5‰ (average 2.1‰) and 1.9–4.4‰ (average 3.5‰), respectively, indicating that $\delta^{34}S_{CDT}$ increases from Py1, through Py2 to Py3. Note that $\delta^{34}S_{CDT}$ of Py1 is mainly in the range of −0.7 to 2.7‰, and only two of the 21 spots are below −4.0‰ (Fig. 13).

6. Discussion

6.1. Origin of pyrites

The phenomenon that colloform pyrite (Py1) and coarse-grained pyrite (Py3) cemented massive magnetite (Fig. 6k) indicates that Py1 and Py3 were formed after magnetite, and that the pyrites (esp. Py1) may have been hydrothermal instead of sedimentary.

The Fe/S ratios of Py1, Py2 and Py3 are 0.882–0.906 (average 0.895), 0.883–0.903 (average 0.892) and 0.837–0.905 (average 0.885), most of which higher than the theoretical value (0.875) (Fig. 14a) and similar to

Fig. 6. Photographs showing representative mineral assemblages and textural features of the Xinqiao deposit. (a) Garnet and diopside replaced by epidote and locally corroded by magnetite (PPL); (b) Epidote among garnets and locally corroded by magnetite (PPL); (c) Epidote locally corrodes garnets (CPL); (d) Magnetite locally replaced radial hematite; (e) Magnetite locally replaced needle-like hematite; (f) Pyrite veins crosscut massive magnetite; (g) Hematite-bearing magnetite replaced along the edges by pyrite; (h) Hand-specimen of colloform pyrites, locally with coarse-grained pyrites; (i) Colloform pyrite rims recrystallized and transformed into fine-grained pyrite, and fine-grained pyrite partially replaced by coarse-grained pyrite; (j) Coarse-grained pyrite vein crosscut colloform pyrite; (k) Coarse-grained pyrite and colloform pyrite cement massive magnetite, indicating that magnetite formed earlier than colloform pyrite; (l) Coarse-grained pyrite coexists with quartz and chalcopyrite in Stage VA; (m) Coarse-grained pyrite replaces magnetite, with some magnetite residues in coarse-grained pyrite; (n) Chalcopyrite-bearing quartz veins crosscut fine-grained pyrite; (o) Chalcopyrite stockwork crosscut coarse-grained pyrite; (p) Pyrrhotite corrodes coarse-grained pyrite; (q) Coarse-grained pyrite + sphalerite + chalcopyrite + quartz veins crosscut quartz-bearing coarse-grained pyrite; (r) The light green, needle-like and transparent minerals resulted from the oxidation of colloform pyrites. Abbreviations: Py1 = colloform pyrite, Py2 = fine-grained pyrite, Py3 = coarse-grained pyrite, Mag = magnetite, Hem = hematite, Ccp = chalcopyrite, Po = pyrrhotite, Sp = sphalerite, Grt = garnet, Di = diopside, Ep = epidote, Qtz = quartz. (For interpretation of the references to color in this figure legend, the reader is referred to the web version of this article.)

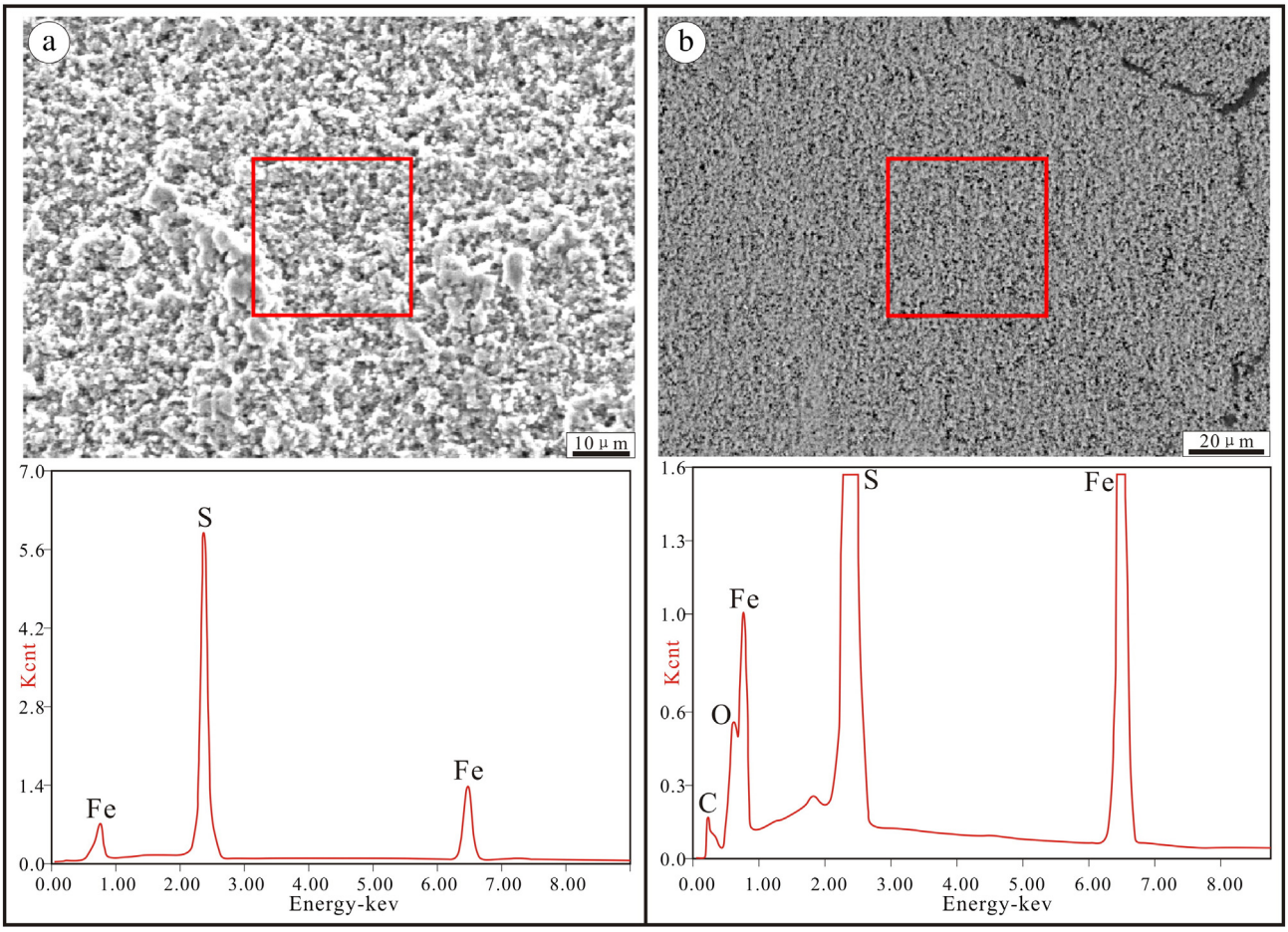

Fig. 8. EDS spectrograms of Py1. (a) EDS spectrogram of Py1 composed of Fe and S; (b) EDS spectrogram of Py1 composed of Fe, S, and also C and O.

the pyrites from magmatic-hydrothermal deposits (e.g., Zhilingtou Au deposit) in China (Mei, 2000).

Song and Zhang (1986) summarized the trace elements characteristics of pyrites from different types of ore deposits in China, and pointed out that the Se/Te ratios of sedimentary pyrites are mainly from 0.2 to 4, while the skarn-type pyrites have a larger range of 0.4 to 75. The Se/Te ratios of Py1 at Xinqiao are 2.39–14.50 (average 7.98), relatively similar to those of skarn-hydrothermal pyrites.

The physicochemical conditions for pyrite formation have an important impact on the pyrite Co and Ni contents and cause different Co/Ni ratios (Hawley and Nichol, 1961; Bralia et al., 1979; Roberts, 1982; Raymond, 1996; Craig et al., 1998; Clark et al., 2004). In general, Co/Ni is below 1 (average 0.63) for sedimentary pyrites (Loftus-Hills and Solomon, 1967), ca. 1–5 for hydrothermal pyrites and ca. 5–50 (average 8.7) for SEDEX-related pyrites (Bralia et al., 1979). The Co/Ni of Py1 ranges from 0.67 to 2.94 (average 1.66), and two of the 13 data are below 1 (Fig. 14b), resembling typical hydrothermal pyrites. The Co/Ni ratios of Py2 and Py3 range from 1.05 to 3.24 (average 1.62) and 1.03 to 4.67 (average 1.66), respectively, also demonstrate hydrothermal affinities.

The $\delta^{34}S_{CDT}$ results (Fig. 15) show that all the three pyrite types and the skarn-type orebodies have similar magmatic-hydrothermal sulfur sources, but obviously different from those of the Upper Carboniferous Huanglong Formation limestone and seawater. However, two Py1 $\delta^{34}S_{CDT}$ values (−4.3‰ and −4.6‰) are distinct from those of the other Xinqiao pyrites and from the skarn-body, but close to those of the Huanglong Formation limestone. Based on the fact that Py1 and

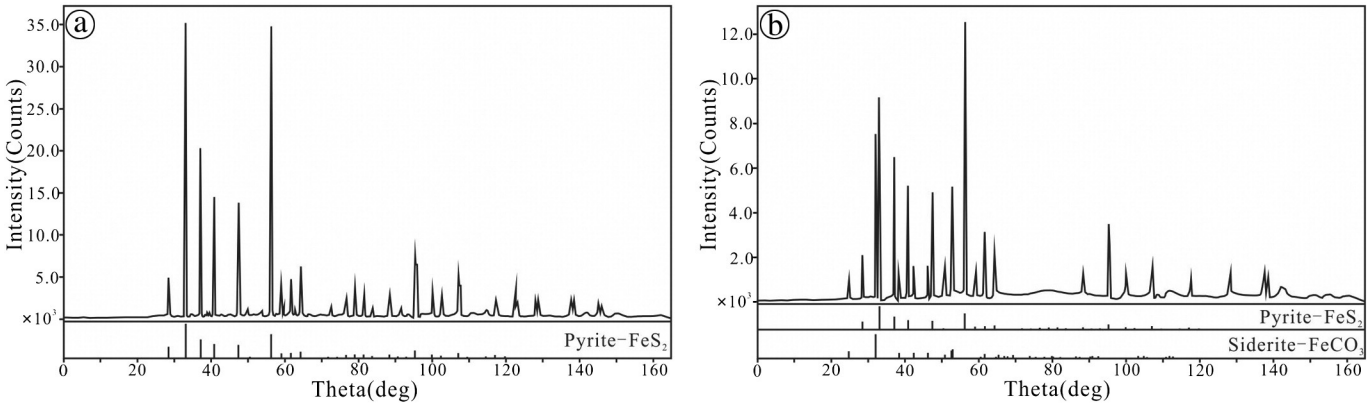

Fig. 9. XRD spectrogram of Py1. (a) XRD spectrogram of Py1 comprises only pyrites; (b) XRD spectrogram of siderites-bearing Py1.

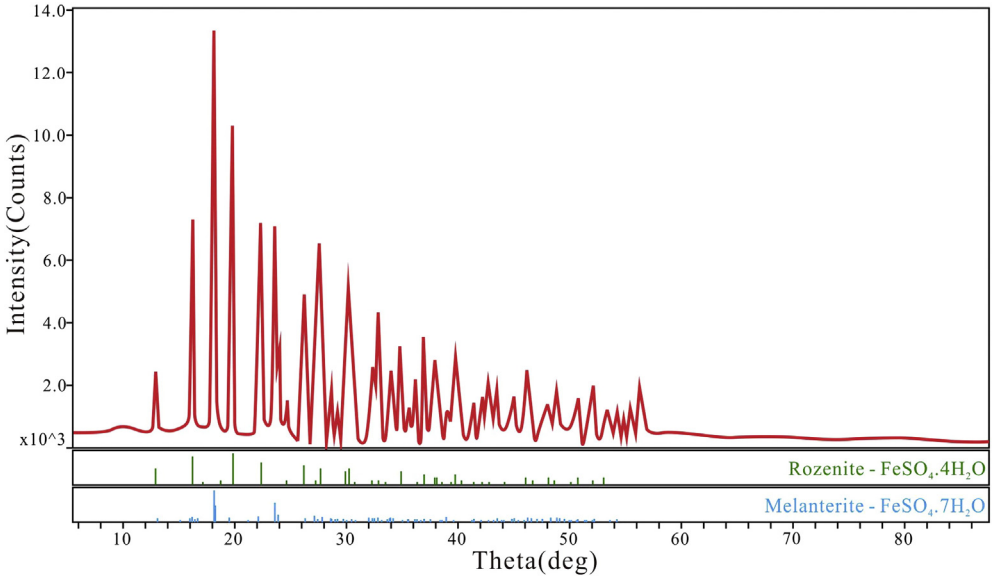

Fig. 10. XRD spectrogram of oxidized Py1, showing the Py1 oxides being rozenite ($FeSO_4 \cdot 4H_2O$) and melanterite ($FeSO_4 \cdot 7H_2O$).

Py3 cement massive magnetite (i.e., Py1 and Py3 formed after magnetite; Fig. 6k), and that Fe/S, Se/Te and Co/Ni ratios for Py1 show a hydrothermal origin, we infer that some Py1 may have inherited its sulfur from the Huanglong Formation limestone via fluid-rock interactions.

Our Fe/S, Co/Ni, Se/Te and sulfur isotope data show that the formation of all the three Xinqiao pyrite types was closely related with magmatic-hydrothermal fluids associated with the Jitou stock, rather than the Huanglong Formation sediments. The colloform texture of pyrite and the sequential development of the colloform ore layers, previously explained by the sedimentation at Xinqiao, have been later found to be rather common in hydrothermal systems, for example at Ezuri in Japan (Barrie et al., 2009). In hydrothermal fluids, the colloform texture represents changes in the physicochemical conditions (Fleet et al., 1989; Craig and Vaughan, 1994), and can be formed during fluid mixing, creating large temperature fluctuations and producing undercooling (Franchini et al., 2015). We infer that the Xinqiao Py1 may reflect rapid crystallization during fluid boiling and/or fluid mixing, creating large temperature fluctuations and producing undercooling in the mixed fluids, which is consistent with previous speculations that Py1 was resulted from rapid crystallization of magmatic-hydrothermal fluids (Meng, 1994, 1996; Ren and Liu, 2006).

Table 1
Representative EMPA geochemical data (wt.%) of the Xinqiao pyrites.
"–": Below the detection limit.

Sample	Minerals	S	Fe	As	Co	Ni	Sb	Ag	Au	Total
XQ11-7	Py1	52.37	47.08	–	0.04	–	–	–	–	99.49
XQ11–7	Py1	51.85	46.54	0.28	0.12	0.04	–	0.01	–	98.83
XQ11–7	Py1	52.62	47.68	–	–	–	–	–	0.05	100.35
XQ43-4	Py1	53.17	46.92	–	–	–	–	0.02	0.01	100.12
XQ43-4	Py1	52.58	47.33	0.16	–	–	0.02	0.02	0.03	100.14
XQ43-4	Py1	51.79	46.51	0.03	0.12	0.01	0.01	0.01	0.07	98.55
XQ43-4	Py1	53.10	46.83	–	0.21	–	0.01	0.01	0.01	100.18
XQ11-7	Py2	52.71	47.46	0.12	0.30	–	0.01	0.03	–	100.63
XQ11-7	Py2	53.45	47.59	–	–	0.02	0.04	–	0.06	101.15
XQ11-7	Py2	52.92	47.79	–	–	–	–	–	0.04	100.75
XQ11-7	Py2	53.18	47.06	–	0.05	–	–	0.01	0.03	100.33
XQ43-4	Py2	52.47	46.97	0.41	0.04	–	0.01	–	–	99.90
XQ43-4	Py2	53.40	47.34	0.15	0.22	–	–	–	0.11	101.22
XQ43-4	Py2	53.04	47.20	0.01	–	0.01	–	0.01	–	100.27
XQ43-9	Py2	52.62	46.46	0.08	0.02	–	–	–	0.11	99.29
XQ43-9	Py2	52.25	46.48	0.02	0.57	–	0.04	–	–	99.36
XQ43-9	Py2	53.47	47.79	–	–	–	–	–	0.15	101.41
XQ11-7	Py3	52.70	47.70	0.22	–	0.01	0.01	0.06	0.10	100.80
XQ11-7	Py3	54.30	45.44	0.38	0.05	0.01	–	–	0.02	100.20
XQ11-7	Py3	53.76	47.04	–	0.05	–	–	–	–	100.84
XQ43-4	Py3	52.22	46.57	1.15	0.02	–	0.02	–	0.13	100.11
XQ43-4	Py3	53.50	46.71	–	–	–	–	–	0.14	100.35
XQ43-4	Py3	52.73	47.39	0.02	0.20	–	0.04	0.02	0.12	100.53
XQ43-4	Py3	53.08	47.82	–	0.05	0.02	–	0.04	–	101.01
XQ43-4	Py3	52.76	46.51	–	0.05	–	–	–	0.09	99.40
XQ43-4	Py3	53.08	46.69	–	–	0.02	–	–	0.03	99.81
XQ43-9	Py3	53.46	47.41	–	0.03	–	–	0.01	–	100.91
XQ43-9	Py3	52.49	46.84	–	0.04	–	–	–	0.19	99.55
XQ43-9	Py3	52.91	47.58	0.06	0.10	–	–	0.02	0.06	100.73

6.2. Occurrences of trace elements in pyrites

Previous studies had documented significant concentrations of Au, Ag, Cu, Pb, Zn, Co, Ni, As, Sb, Se, Te, Hg, Tl and Bi in pyrite (Cook and Chryssoulis, 1990; Reich et al., 2005; Reich and Becker, 2006; Large et al., 2009; Deditius et al., 2011; Reich et al., 2013). Modes of trace metal occurrences in pyrite include: (1) Solid solution within the crystal lattice; (2) In sulfide nanoparticles; (3) In micron-sized sulfide inclusions; (4) In micron-sized silicate or oxides inclusions (Thomas et al., 2011; Ciobanu et al., 2012; Zhang et al., 2014). Nickel and Co are readily incorporated into the pyrite lattice via isomorphous replacement of Fe, and are not readily released during hydrothermal pyrite recrystallization, while As, Se and Te enter the lattice by replacing sulfur (Huerta-Diaz and Morse, 1992; Morse and Luther, 1999; Tribovillard et al., 2006; Large et al., 2009; Koglin et al., 2010). Lead does not enter the pyrite crystal lattice readily due to its large ionic size, and has a faster precipitation rate from an aqueous solution as metal sulfide when compared to Fe, which leads to an earlier formation of galena than pyrite, and to the common presence of galena inclusions in pyrites (Huerta-Diaz and Morse, 1992; Morse and Luther, 1999; Koglin et al., 2010).

Molybdenum, Bi, Cu, Pb and Sb, plus minor Zn, W, Sn, Ag and Au are the mineralized elements in the Xinqiao pyrites. Lead and Bi in the Xinaqiao pyrites have a positive correlation (Fig. 16a), and Pb/Co has a more distinct positive correlation relationship with Ag/Co (Fig. 16b) and Bi/Co (Fig. 16c). Since Co enters the pyrite lattice readily and Pb occurs as galena inclusions in pyrites, the good positive correlations between Pb/Co and Ag/Co, Bi/Co might also imply that Ag and Bi occur mainly as minute inclusions in pyrites.

Gold and As concentrations of pyrites in hydrothermal ore deposits can constrain the saturation state of Au-bearing fluids from which As-bearing pyrite precipitated, and provide information of Au distribution in pyrite (Reich et al., 2005). For the Xinaqiao pyrites, Au and As

Table 2
Representative LA-ICP-MS trace elements data (ppm) of the Xinqiao pyrites.
"–": Below the detection limit.

Sample	Minerals	V	Cr	Mn	Co	Ni	Cu	Zn	Ga	As	Se	Mo	Ag
XQ11-7	Py1	4.03	0.80	237.36	1.13	1.61	1166.58	34.76	0.35	624.75	–	289.62	57.32
XQ11-7	Py1	2.31	–	139.60	2.26	1.06	1129.45	1.48	0.19	730.03	0.79	188.43	60.02
XQ11-7	Py1	3.02	0.37	246.04	2.02	1.13	985.63	2.89	0.27	639.71	–	155.65	52.47
XQ11-7	Py1	5.69	0.17	114.16	1.64	1.07	663.22	1.33	0.59	401.03	1.49	43.92	48.07
XQ43-4	Py1	2.11	–	65.18	1.41	0.48	726.24	–	0.13	219.79	1.07	47.46	60.35
XQ43-4	Py1	1.59	–	55.45	0.90	0.53	887.93	–	–	266.45	–	30.69	60.98
XQ43-4	Py1	6.00	0.33	65.22	2.33	3.46	972.55	–	0.92	373.64	–	31.01	68.46
XQ43-9	Py1	56.58	0.76	1352.67	1.35	1.24	250.53	144.55	2.96	608.40	4.64	50.47	8.65
XQ43-9	Py1	34.04	0.48	563.14	2.26	1.35	329.59	17.66	4.12	751.99	2.58	36.88	16.39
XQ43-9	Py1	7.81	1.16	345.55	2.19	1.22	277.37	21.29	1.09	782.99	2.18	14.17	20.33
XQ43-9	Py1	10.65	4.24	257.24	2.07	1.39	450.72	1.56	9.93	238.59	1.74	0.45	30.22
XQ43-9	Py1	2.73	1.34	24.49	2.31	2.07	703.68	–	2.57	430.15	1.78	3.55	40.26
XQ43-9	Py1	24.80	0.82	243.11	1.85	0.64	591.09	4.16	10.46	867.95	0.97	1.11	27.99
XQ11-7	Py2	0.13	–	11.31	36.65	7.85	2.93	2.74	0.09	13.15	13.56	0.29	0.09
XQ11-7	Py2	44.93	1.95	2671.82	2.52	1.92	243.42	112.36	1.16	659.20	0.58	20.02	10.02
XQ11-7	Py2	4.42	40.96	1435.43	2.13	2.07	345.04	15.12	2.05	3015.46	–	0.99	10.79
XQ43-4	Py2	1.83	2.48	2362.09	0.76	0.63	1250.23	–	1.13	481.39	1.55	17.25	9.32
XQ43-4	Py2	1.06	0.28	1200.43	0.94	0.76	1765.30	–	14.89	383.01	3.13	26.15	11.97
XQ43-4	Py2	0.87	0.32	1073.31	1.31	1.18	1108.19	–	0.84	361.52	5.72	7.59	8.68
XQ43-9	Py2	0.01	–	1.75	13.71	13.09	4.33	–	–	237.88	–	–	0.86
XQ11–7	Py3	6.70	2.35	169.21	1.69	1.11	192.78	13.29	0.23	2525.71	1.64	11.68	10.70
XQ11-7	Py3	4.75	–	112.96	1.83	0.82	64.94	4.93	0.35	793.02	–	0.28	6.32
XQ11-7	Py3	10.56	1.17	297.79	1.78	1.36	157.04	4.22	0.19	1994.82	0.65	10.86	18.13
XQ11-7	Py3	0.63	0.16	102.26	0.82	0.61	8872.70	–	0.26	484.23	4.47	1.16	19.46
XQ43-4	Py3	2.10	–	86.92	0.92	0.63	77.42	–	–	391.01	–	0.77	2.55
XQ43-4	Py3	0.14	–	3.18	1.34	1.28	1956.46	–	0.14	–	–	0.07	1.10
XQ43-4	Py3	4.52	0.26	99.94	1.11	0.56	136.74	–	0.59	1680.89	–	2.20	7.17
XQ43-9	Py3	0.56	0.90	9.72	3.07	2.44	1276.50	–	0.30	87.75	–	0.07	2.94
XQ43-9	Py3	8.55	0.07	165.77	1.35	0.89	411.36	–	0.23	406.94	2.19	1.91	8.59
XQ43-9	Py3	7.70	0.78	191.41	1.46	1.36	258.74	10.89	1.86	168.84	–	0.67	18.88
XQ43-9	Py3	3.86	1.45	9.10	1.69	1.26	7.05	–	9.63	15.30	0.77	0.05	3.23
XQ43-9	Py3	0.07	–	–	1.37	1.17	2.90	3.08	–	9.86	14.92	–	0.04
XQ43-9	Py3	0.83	1.11	6975.45	63.32	19.53	43.50	5.24	0.44	310.97	–	0.05	1.93
XQ43-9	Py3	0.20	0.30	10.42	24.03	11.23	1145.13	49.51	0.11	13.28	–	–	0.51

Sample	Minerals	Cd	In	Sn	Sb	Te	Ba	W	Au	Hg	Tl	Pb	Bi
XQ11-7	Py1	0.42	0.02	0.07	182.24	0.08	2.43	0.48	0.05	0.32	6.89	938.35	296.24
XQ11-7	Py1	0.03	–	0.41	160.25	0.33	0.41	0.61	0.10	0.31	5.22	1060.32	275.53
XQ11-7	Py1	0.07	0.03	0.57	203.28	–	0.24	0.62	0.03	–	5.11	880.36	324.76
XQ11-7	Py1	–	0.04	0.18	88.74	0.15	0.15	0.85	0.03	0.08	5.00	1790.02	252.05
XQ43-4	Py1	–	0.02	0.15	95.92	0.21	0.03	0.16	0.02	0.16	3.30	885.14	267.99
XQ43-4	Py1	–	0.02	0.10	105.37	0.66	0.01	0.09	0.05	0.26	3.91	1028.72	266.80
XQ43-4	Py1	0.04	0.03	0.05	137.06	0.34	0.11	0.65	0.05	0.24	4.88	1536.28	435.92
XQ43-9	Py1	–	0.18	1.38	31.32	–	20.62	12.99	0.03	1.16	6.58	734.58	174.61
XQ43-9	Py1	0.26	0.06	1.93	35.21	–	6.56	9.97	0.04	0.52	5.54	677.00	201.49
XQ43-9	Py1	–	0.01	0.29	32.54	–	8.73	1.10	0.01	0.30	6.22	507.11	196.28
XQ43-9	Py1	–	0.03	0.80	30.55	0.12	4.64	1.56	0.05	0.55	17.58	767.50	342.98
XQ43-9	Py1	–	–	0.31	41.66	–	14.06	1.53	0.09	0.44	13.83	1951.79	500.47
XQ43-9	Py1	–	0.06	1.19	41.23	–	14.25	2.77	0.04	0.91	31.45	1217.79	525.75
XQ11-7	Py2	–	–	0.28	–	–	0.67	0.77	0.58	1.94	0.31	0.50	1.63
XQ11-7	Py2	0.39	0.29	0.31	34.55	–	0.15	4.56	–	0.65	11.45	547.74	123.81
XQ11-7	Py2	0.31	0.25	0.92	1.96	6.48	0.26	0.46	0.65	0.60	3.36	52.79	59.10
XQ43-4	Py2	0.14	0.10	1.36	333.98	0.17	7.82	8.89	0.05	0.18	4.29	1260.69	4.65
XQ43-4	Py2	–	0.02	3.45	263.12	–	6.77	3.46	0.05	0.37	4.87	1358.74	4.35
XQ43-4	Py2	–	0.01	0.64	276.63	–	8.99	4.59	–	0.49	3.83	1277.80	3.15
XQ43-9	Py2	0.79	–	–	0.05	5.69	0.12	–	–	–	0.04	2.51	9.54
XQ11-7	Py3	–	0.01	0.04	5.92	–	10.61	0.94	0.11	1.13	17.52	111.12	90.02
XQ11-7	Py3	–	0.01	–	0.85	0.13	9.86	1.43	0.03	0.43	2.92	50.58	30.27
XQ11-7	Py3	–	–	0.06	1.65	0.81	0.79	1.22	0.22	0.88	5.21	101.58	134.17
XQ11-7	Py3	0.28	0.08	–	6.66	–	–	0.09	0.58	–	5.08	93.41	5.16
XQ43-4	Py3	0.05	–	–	0.38	0.22	0.03	0.08	–	0.61	0.85	10.50	4.97
XQ43-4	Py3	–	–	0.11	0.12	0.65	–	0.08	–	0.33	0.18	5.52	0.99
XQ43-4	Py3	–	0.01	0.03	1.31	–	0.03	0.13	–	0.03	6.64	60.36	18.53
XQ43-9	Py3	–	–	0.20	1.87	0.13	0.03	0.14	–	–	0.34	48.72	5.02
XQ43-9	Py3	–	–	–	3.55	–	4.21	0.44	0.01	1.63	56.40	127.22	5.83
XQ43-9	Py3	–	–	0.15	20.14	–	4.47	0.72	0.09	0.62	22.96	367.90	224.75
XQ43-9	Py3	–	–	0.06	0.18	–	2.75	–	0.05	–	0.56	13.83	5.15
XQ43-9	Py3	–	0.02	–	0.05	2.29	1.93	0.01	–	0.34	–	–	–
XQ43-9	Py3	–	0.08	0.39	1.11	–	2.83	0.30	–	–	–	49.44	2.35
XQ43-9	Py3	0.61	0.28	0.04	–	10.46	0.32	0.51	0.41	1.82	0.19	3.30	4.82

concentrations plot above the solubility limit of the solid solution for Au (Fig. 17), indicating that the Au probably occurs as Au^0 (Au nanoparticles) in pyrites.

Zhou et al. (2010) and Xiao et al. (2016) pointed out that the concentrations of Cu, Pb, Zn, Au and Ag in Py2 and Py3 are higher than in Py1, and that these metals may have mostly come from the Jurassic-Cretaceous

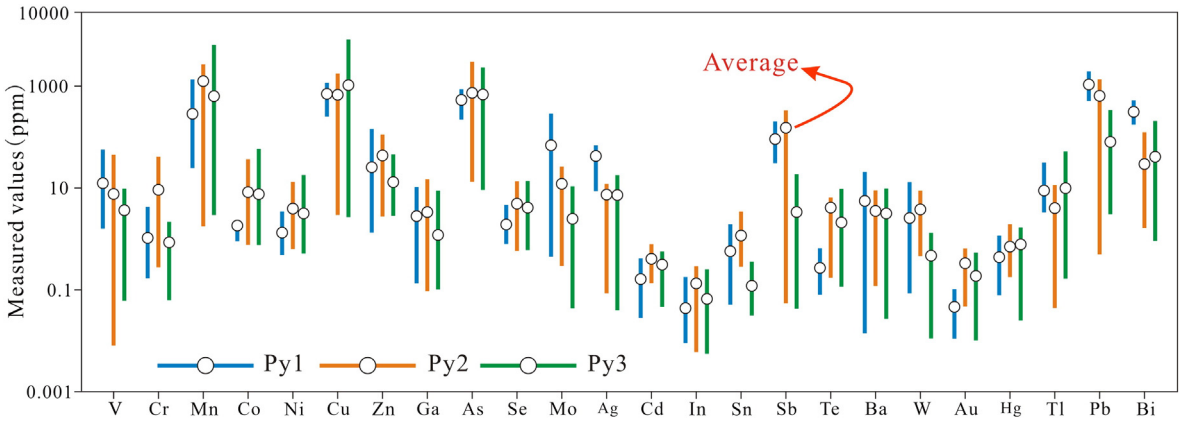

Fig. 11. Trace elements concentration diagram of the Xinqiao pyrites.

Table 3
Concentrations ranges (ppm) of Mn, Cu, As, Co and Ni of the Xinqiao pyrites.
Data in the parentheses: The average concentrations (ppm).

	Mn	Cu	As	Co	Ni
Py1	24.49–1353 (285)	251–1167 (703)	220–868 (534)	0.90–2.33 (1.82)	0.48–3.46 (1.33)
Py2	1.75–2672 (125)	2.93–1765 (674)	13.15–3015 (736)	0.76–36.65 (8.29)	0.63–13.09 (3.93)
Py3	3.18–6975 (633)	2.90–8873 (1043)	9.86–2526 (683)	0.82–63.32 (7.56)	0.56–19.53 (3.16)

magmatic-hydrothermal fluids associated with the Jitou stock. Our study has generated more detailed data. Cu (average 674 and 1043 ppm, respectively) and Au (average 0.33 and 0.19 ppm, respectively) concentrations in Py2 and Py3 are higher than in Py1 (average: 702 ppm Cu and 0.05 ppm Au), Zn (average 25.52 ppm) in Py1 is close to the values (average 43.41 and 13.02 ppm, respectively) in Py2 and Py3, and Ag (average 42.42 ppm) and Pb (average 1075 ppm) in Py1 are markedly higher than in Py2 (average: 7.39 ppm Ag and 643 ppm Pb) and Py3 (average: 7.25 ppm Ag and 80 ppm Pb). We infer that these geochemical differences among the various Xinqiao hydrothermal pyrites are the results of different composition and/or physicochemical conditions of relevant hydrothermal fluids. Such geochemical differences also suggest that for these pyrites, Stage IV is the main Ag enrichment stage, whereas Stage V is the main Cu-Au enrichment stage.

6.3. Metallogenic implications for the Xinqiao deposit

6.3.1. Genesis of the footwall stockwork mineralization

As mentioned above, three hypotheses for the Xinqiao mineralization were proposed, with the major controversies focusing on whether: 1) the colloform pyrites were of magmatic-hydrothermal or sedimentary origin, and 2) the footwall stockwork mineralization was of Jurassic-Cretaceous magmatic-hydrothermal or Late Paleozoic submarine exhalation (channel-way product) origin. For the first issue, the evidence outlined in the discussion sections above has clearly supported a hydrothermal origin for the Xinqiao colloform pyrite.

The footwall stockwork mineralization of the stratiform orebody is dominated by pyrite-quartz veins (Fig. 4a), distinct from the mineral assemblage (such as anhydrite and barite) in typical SEDEX footwall stockwork mineralization (Sangster, 1990). More importantly, the footwall alteration of the Xinqiao stratiform orebody is dominated by silicification, inconsistent with typical SEDEX deposits, which is characterized by tourmaline, albitite, chlorite and epidote alterations (Sangster, 1990).

In addition, if the stratiform orebody formed during the Late Paleozoic submarine exhalation, the parallel unconformity interface that hosts the stratiform orebody would have occurred in an epicontinental or shallow sea environment, considerably shallower than the formation depths (deep seafloor: 1.5–3.5 km; Scott, 2008) of SEDEX (Mao et al., 2009). Moreover, typical SEDEX deposits are characterized by syngenetic mineralization, but there is a clear abrupt contact interface

Table 4
In situ sulfur isotope data (‰) by SHRIMP of the Xinqiao pyrites.

Sample	Spot	Minerals	$\delta^{34}S_{CDT}$	Std error	Sample	Spot	Minerals	$\delta^{34}S_{CDT}$	Std error
XQ11-7	1	Py2	1.75	0.05	XQ43-4	16	Py2	1.93	0.05
XQ11-7	2	Py3	4.38	0.05	XQ43-4	17	Py1	−4.32	0.05
XQ11-7	3	Py3	4.16	0.05	XQ43-4	18	Py1	2.44	0.04
XQ11-7	4	Py2	2.05	0.05	XQ43-4	19	Py1	0.82	0.05
XQ11-7	5	Py1	−0.62	0.04	XQ43-4	20	Py1	2.74	0.05
XQ11-7	6	Py3	3.74	0.05	XQ43-4	21	Py1	1.29	0.04
XQ11-7	7	Py1	1.71	0.05	XQ43-9	22	Py1	0.50	0.04
XQ11-7	8	Py1	2.29	0.05	XQ43-9	23	Py1	0.85	0.04
XQ11-7	9	Py1	−0.06	0.05	XQ43-9	24	Py1	1.79	0.04
XQ11-7	10	Py3	3.55	0.05	XQ43-9	25	Py1	1.99	0.05
XQ11-7	11	Py1	0.74	0.04	XQ43-9	26	Py1	1.15	0.04
XQ43-4	12	Py2	2.45	0.04	XQ43-9	27	Py1	−0.67	0.04
XQ43-4	13	Py1	1.36	0.04	XQ43-9	28	Py1	−4.61	0.05
XQ43-4	14	Py1	2.25	0.04	XQ43-9	29	Py1	−0.21	0.06
XQ43-4	15	Py3	1.88	0.05	XQ43-9	30	Py1	0.77	0.06

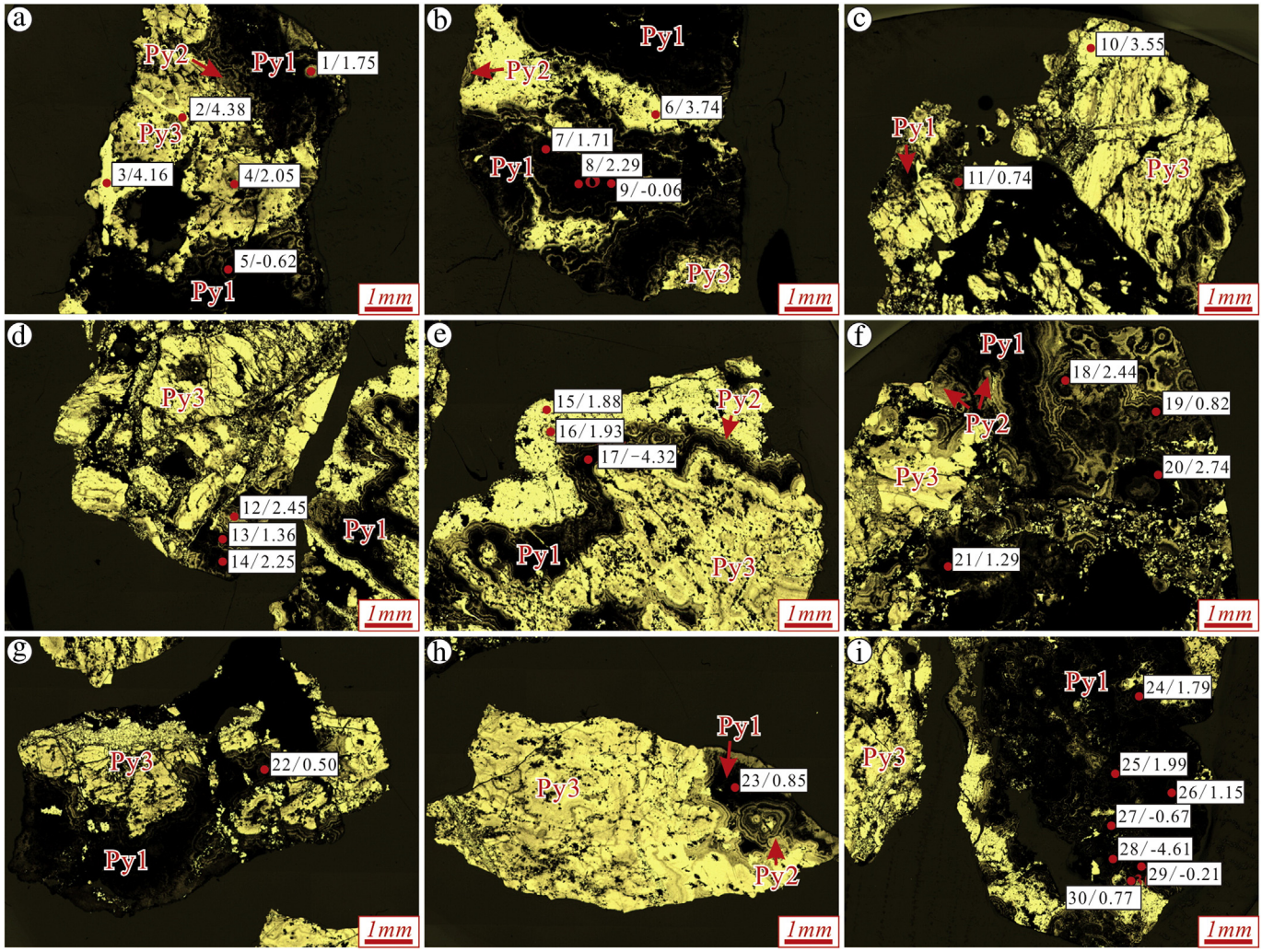

Fig. 12. Analytical spot locations and values of the in situ sulfur isotope analysis by SHRIMP for the Xinqiao pyrites (‰). (Analysis spot/$\delta^{34}S_{CDT}$). Abbreviations: Py1 = colloform pyrite, Py2 = fine-grained pyrite, Py3 = coarse-grained pyrite.

between the Xinqiao stratiform orebody and the Wutong Formation quartz sandstone (Fig. 4b), indicative of epigenetic mineralization.

Although the Re-Os isochron age (319 ± 13 Ma; Guo et al., 2011) of pyrites from the footwall pyrite-bearing quartz veins may imply the Late Paleozoic submarine exhalation origin for the Xinqiao deposit, the initial value of $^{187}Os/^{188}Os$ (0.017) is inconsistent with the initial $^{187}Os/^{188}Os$ of typical SEDEX deposits, which usually lie in the range between average oceanic crust (~1) and seawater (~8) (Ravizza et al., 1996). The ^{187}Os vs. ^{187}Re ratios of pyrites plot in a fairly narrow field, which do not meet the conditions of Re-Os isochron age and most likely reflect the true age of the footwall stockwork mineralization (Huang, 2011).

In addition, Zhang (2015) pointed out that the $\delta^{34}S_{CDT}$ of Py3 from the footwall stockwork mineralization is of 2.8–3.8‰ (average 3.3‰), close to that of the Jitou stock-related skarn mineralization (2.7‰ to 4.3‰, average 3.3‰) and disseminated pyrite in the Jitou stock (2.8‰ to 4.5‰, average 3.4‰), but clearly distinct from the Upper Carboniferous Huanglong Formation limestone (−9.47‰ to −15.42‰; Tang et al., 1998). Similarly, the footwall stockwork mineralization yielded an initial $^{87}Sr/^{86}Sr$ ratio of 0.71138 ± 0.00014 (Zhang, 2015), similar to those of the stratiform orebody (0.710; Li et al., 1997) and the Jitou stock (0.7065; Yu et al., 1998) but different from that of the ore-hosting limestone (0.7246; Zhang, 2015). Therefore, we conclude that the footwall stockwork mineralization is likely to be genetically linked to the magmatic-hydrothermal fluids associated with the Jitou stock.

6.3.2. Mineralization of the Xinqiao deposit

Based on the discussion above, we conclude that the stratiform orebody (including the footwall stockworks) at Xinqiao was likely to

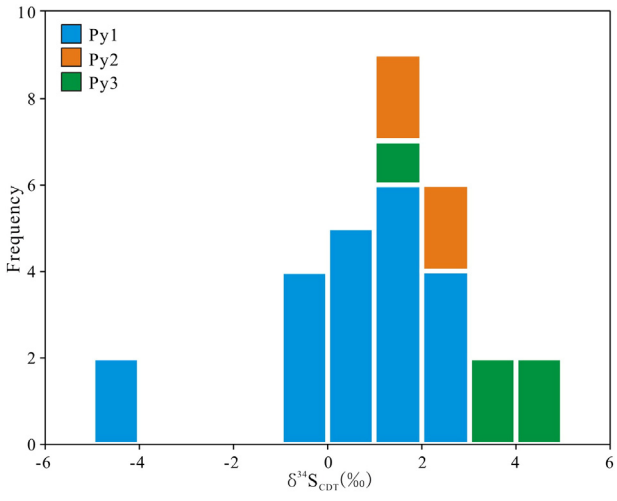

Fig. 13. Sulfur isotope histogram for the Xinqiao pyrites, in-situ analyzed by SHRIMP.

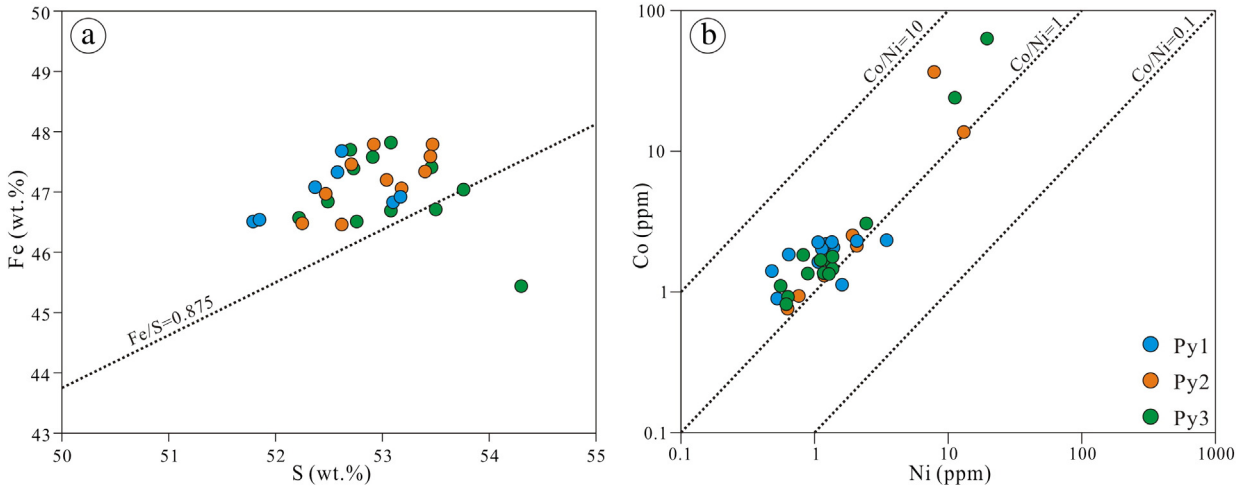

Fig. 14. (a) Fe vs. S diagram for the Xinqiao pyrites. (b) Co vs. Ni diagram for the Xinqiao pyrites.

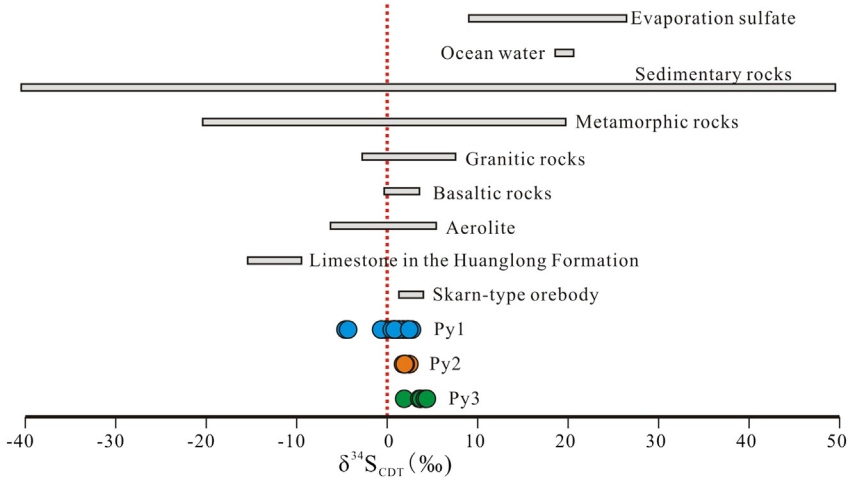

Fig. 15. Sulfur isotope composition diagram for the Xinqiao deposit ($\delta^{34}S_{CDT}$ of the Huanglong Formation limestone from Tang et al. (1998), and $\delta^{34}S_{CDT}$ of the skarn-type orebodies from Zang et al. (2004).

form from Jurassic-Cretaceous magmatic-hydrothermal fluids, probably associated with the nearby Jitou stock, and the Xinqiao Cu-S-Fe mineraization may have been generated by the Yanshanian tectono-thermal event in Eastern China.

From ca. 180 to 90 Ma, the continental margin of Eastern China may have evolved from an active continental margin to an intraplate setting, and the stress field may have changed from compressive to extensional (Qi et al., 2000). When the subduction of the paleo-Pacific plate began and the continental crust of the Yangtze Craton delaminated, the structural orientation of the MLYB may have changed from E–W to NE–SW trending, and then to NNE–SSW trending (Zhou et al., 2008), and the resultant complex crustal-mantle interactions may have generated intense

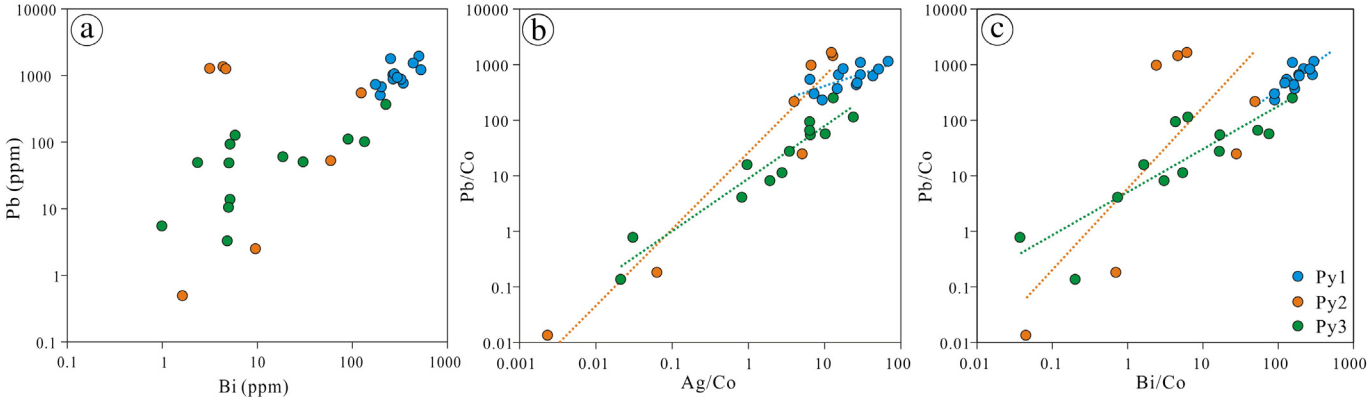

Fig. 16. Scatter diagrams of (a) Pb vs. Bi, (b) Pb/Co vs. Ag/Co and (c) Pb/Co and Bi/Co of the Xinqiao pyrites.

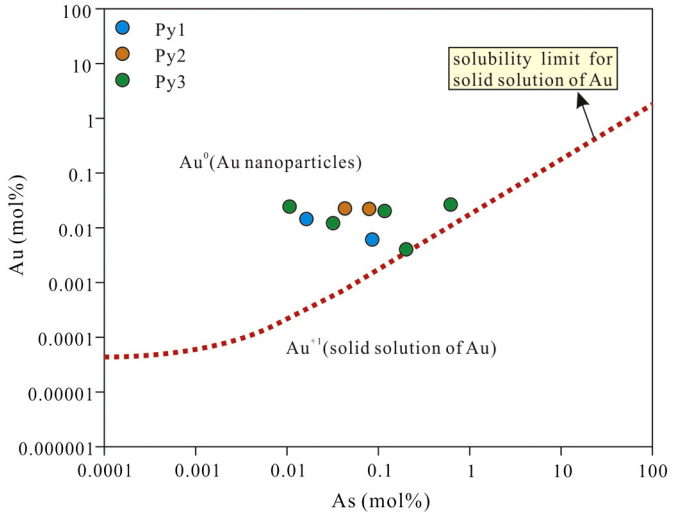

Fig. 17. Correlation diagram of Au and As concentrations in the Xinqiao pyrites, showing that the Au probably occurs as Au^0 (Au nanoparticles) in the pyrites.

magmatism (Mao et al., 2003; Wu et al., 2003). Under such a tectono-magmatic regime, the region between the Jitou–Shatanjiao basement fault and the NNE–SSW-trending fault zone was stretched, leading to the magma from the lower crust upwelling (Zhang, 2015). The magmas may have migrated along the NE-trending Dachengshan anticline and the NNE-trending Shenchong syncline to form the NW-trending Jitou stock (Liu et al., 1996). Subsequently, magmatic-hydrothermal fluids enriched in ore-forming elements (e.g., Cu, S, and Fe) may have ascended and entered the detachments between the Upper Devonian Wutong Formation quartz sandstone and the Upper Carboniferous Huanglong Formation limestone in the Early Cretaceous (ca. 138.0 ± 2.3 Ma, Rb-Sr isotope isochron age for the quartz fluid inclusions from the footwall stockwork mineralization;. This may have led to the early (Stage I) and late (Stage II) skarn alterations. With decreasing temperature, Fe in the ore-forming fluids precipitated to form hematite and magnetite (Stage III). The Fe-oxides mineralization and the fluid mixing had substantially altered the physicochemical conditions of the ore fluids, and generated large temperature fluctuations and undercooling, resulting in the rapid crystallization of Stage IV colloform pyrites (Py1) that locally cemented the early massive magnetite. Continuous influx of the ore-forming fluids and temperature drop may have led to the formation of abundant quartz, fine to coarse-grained pyrites (Py2 and Py3) and chalcopyrite with local pyrrhotite, galena, sphalerite, sericite, chlorite and calcite (Stage V) in the stratiform orebody. Coevally, some ore-forming fluids may have entered the Wutong Formation quartz sandstone to form the stockwork mineralization (Fig. 18; Zhang, 2015).

7. Conclusion

(1) Hydrothermal alteration and mineralization at Xinqiao comprises five stages, including garnet and diopside alteration (Stage I), epidote alteration (Stage II), hematite (Stage IIIA) and magnetite (Stage IIIB) mineralization, colloform pyrite (Stage IV) mineralization and quartz-sulfides (Stage V) mineralization.
(2) SEM imagery for colloform pyrites reveals that single colloform pyrite grains are composed of cubic microcrystalline pyrite aggregates, and EDS and XRD data indicate that some colloform pyrites contain minor siderite impurities.

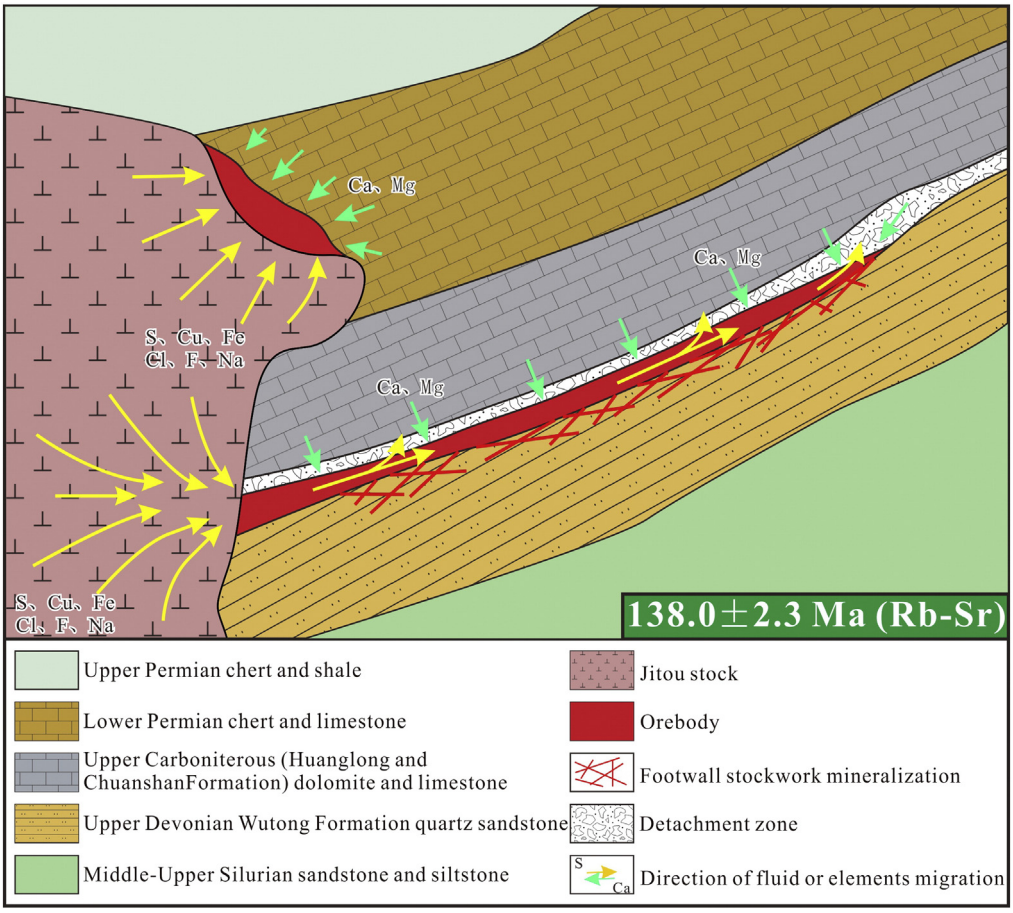

Fig. 18. Genetic model of the Xinqiao Cu-S-Fe deposit.

(3) For the pyrites from the Xinqiao stratiform orebody, Ag and Bi occur mainly as inclusions and Au occurs as Au^0 (Au nanoparticles).
(4) The Fe/S, Se/Te and Co/Ni values of the Py1 display typical hydrothermal affinities. In-situ SHRIMP sulfur isotope data reveals that the Py1 $\delta^{34}S_{CDT}$ (−0.6‰ to 2.7‰, average 0.6‰) values are close to those of the skarn-type orebodies, but distinct from those of the Upper Carboniferous Huanglong Formation limestone, suggesting that Py1 may have been genetically linked to the Jurassic-Cretaceous magmatic-hydrothermal fluids associated with the Jitou stock.
(5) The Xinqiao stratiform orebody may have been formed from Jurassic-Cretaceous magmatic-hydrothermal fluids associated with the Jitou stock, similar to the skarn-type orebodies.

Conflict of interest

We declare that we have no financial and personal relationships with other people or organizations that can inappropriately influence our work, there is no professional or other personal interest of any nature or kind in any product, service and/or company that could be construed as influencing the position presented in, or the review of, the manuscript entitled.

Acknowledgements

This research was jointly funded by the Project of Innovation-driven Plan of the Central South University (2015CX008), the Special Research Funding for the Public Benefit of the MLR China (200911007-4) and CAS/SAFEA International Partnership Program for Creative Research Teams (20140491534). We especially thank Dr Zhang Jian-dong for the LA-ICP-MS trace elements analysis, Professor Gu Xiang-ping for assisting the XRD analysis and Professor Trevor Ireland and Dr Janaina Avila for the SHRIMP sulfur isotope analysis. We sincerely appreciate the detailed and constructive reviews and suggestions from Dr Mark Pearce and Prof Taofa Zhou, which greatly improved this paper. Dr Yanhua Zhang is thanked for the editorial help.

References

#803 Geological Brigade of East China Metallurgical and Geological Exploration, 1971. Internal Exploration Report for the Xinqiao Deposit (in Chinese).
Barrie, C.D., Boyce, A.J., Boyle, A.P., Williams, P.J., Blake, K., Ogawara, T., Akai, J., Prior, D.J., 2009. Growth controls in colloform pyrite. Am. Mineral. 94, 415–429.
Bralia, A., Sabatini, G., Troja, F., 1979. A revaluation of the Co/Ni ratio in pyrite as geochemical tool in ore genesis problems. Mineral. Deposita 14, 353–374.
Chang, Y.F., Liu, X.G., 1983. Layer control type skarn type deposit—some deposits in the Middle-Lower Yangtze Depression in Anhui Province as an example. Mineral. Deposita 2 (1), 11–20 (in Chinese).
Chang, Y.F., Liu, X.P., Wu, Y.Z., 1991. Metallogenic Belt of the Middle-Lower Yangtze River. Geological Publishing House, Beijing, pp. 1–379 (in Chinese).
Ciobanu, C.L., Cook, N.J., Utsunomiya, S., Kogagwa, M., Green, L., Gilbert, S., Wade, B., 2012. Gold-telluride nanoparticles revealed in arsenic-free pyrite. Am. Mineral. 97, 1515–1518.
Clark, C., Grguric, B., Mumm, A.S., 2004. Genetic implications of pyrite chemistry from the Paleoproterozoic Olary Domain and overlying Neoproterozoic Adelaidean sequences, northeastern South Australia. Ore Geol. Rev. 25, 237–257.
Cook, N.J., Chryssoulis, S.L., 1990. Concentrations of invisible gold in the common sulfides. Can. Mineral. 28, 1–16.
Cook, N.J., Ciobanu, C.L., Mao, J., 2009. Textural control on gold distribution in As-free pyrite from the Dongping, Huangtuliang and Hougou gold deposits, North China Craton (Hebei Province, China). Chem. Geol. 264, 101–121.
Craig, J.R., Vaughan, D.J., 1994. Ore Microscopy and Ore Petrography. second ed. John Wiley and Sons Inc., p. 423.
Craig, J.R., Vokes, F.M., Solberg, T.N., 1998. Pyrite: physical and chemical textures. Mineral. Deposita 34, 82–101.
Deditius, A., Utsunomiya, S., Reich, M., Kesler, S.E., Ewing, R.C., Hough, R., Walshe, J., 2011. Trace metal nanoparticles in pyrite. Ore Geol. Rev. 42, 32–46.
Fleet, M.E., MacLean, P.J., Barbier, J., 1989. Oscillatory-zoned As-bearing pyrite from strata-bound and stratiform gold deposits: an indicator of ore fluid evolution. In: Keays, R.R., Ramsay, W.R.H., Groves, D.I. (Eds.), The Geology of Gold: The Perspective in 1988. Econ. Geol Vol. 6, pp. 356–362.
Franchini, M., McFarlane, C., Maydagan, L., Reich, M., Lentz, D.R., Meinert, L., Bouhier, V., 2015. Trace metals in pyrite and marcasite from the Agua Rica porphyry-high sulfidation epithermal deposit, Catamarca, Argentina: textural features and metal zoning at the porphyry to epithermal transition. Ore Geol. Rev. 66, 366–387.
Fu, S.G., Yan, X.Y., Yuan, C.X., 1977. Geologic feature of submarine volcanic eruption- sedimentary pyrite type deposit in Carboniferous in the Middle–Lower Yangtze River Valley metallogenic belt, Eastern China. J. Nanjing Univ. Nat. Sci. Ed. 4, 43–67 (in Chinese).
Gregory, D.D., Large, R.R., Halpin, J.A., Steadman, J.A., Hickman, A.H., Ireland, T.R., Holden, H., 2014. The chemical conditions of the late Archean Hamersley basin inferred from whole rock and pyrite geochemistry with $\Delta^{33}S$ and $\delta^{34}S$ isotope analyses. Geochim. Cosmochim. Acta 149, 223–225.
Gu, L.X., Hu, W.X., He, J.X., 2000. Regional variations in ore composition and fluid features of massive sulfide deposits in South China: implications for genetic modeling. Episodes 23 (2), 110–118.
Gu, L.X., Xu, K.Q., 1986. On the Carboniferous submarine massive sulfide deposit in the lower reaches of the Yangtze River. Acta Geol. Sin. 60 (2), 176–188 (in Chinese).
Guo, W.M., Lu, J.J., Jiang, S.Y., Zhang, R.Q., Qi, L., 2011. Re-Os isotope dating of pyrite from the footwall mineralization zone of the Xinqiao deposit, Tongling, Anhui Province: geochronological evidence for submarine exhalative sedimentation. Chin. Sci. Bull. 56 (36), 3860–3865 (in Chinese with English abstract).
Hawley, J.E., Nichol, I., 1961. Trace element in pyrite, pyrrhotite and chalcopyrite of different ore. Econ. Geol. 56 (3), 467–487.
Huang, G.H., 2011. Mineralization Characteristics and Genesis of Xinqiao Cu-S-Au Polymetallic Deposit, Tongling, Anhui Province, China Master Thesis China University of Geosciences, Wuhan (in Chinese with English abstract).
Huerta-Diaz, M.A., Morse, J.W., 1992. Pyritization of trace metals in anoxic marine sediments. Geochim. Cosmochim. Acta 56, 2681–2702.
Ireland, T.R., Schram, N., Holden, P., Lanc, P., Avila, J., Armstrong, R., Amelin, Y., Latimore, A., Corrigan, D., Clement, S., Foster, J., Compston, W., 2014. Charge-mode electrometer measurements of S-isotopic compositions on SHRIMP-SI. Int. J. Mass Spectrom. 359, 26–37.
Koglin, N., Frimmel, H.E., Minter, W.E.L., Brätz, H., 2010. Trace-element characteristics of different pyrite types in Mesoarchaean to Paleoproterozoic placer deposits. Mineral. Deposita 45, 259–280.
Large, R.R., Danyushevsky, L.V., Hollit, C., Maslennikov, V., Meffre, S., Gilbert, S.E., Bull, S., Scott, R.J., Emsbo, P., Thomas, H., Singh, B., Foster, J., 2009. Gold and trace element zonation in pyrite using a laser imaging technique: implications for the timing of gold in orogenic and Carlin-style sediment-hosted deposits. Econ. Geol. 104, 635–668.
Li, W.D., Wang, W.B., Fang, H.Y., 1997. Ore-forming conditions of Cu (Au) deposit-intensive areas and existence possibility of super large ore deposit in the Middle-Lower Yangtze River Valley metallogenic belt. Volcanol. Mineral. Res. 20 (s), 1–131.
Liu, W.C., Gao, D.Z., Chu, G.Z., 1996. Analysis of Tectonic Deformation and Metallogenic Prediction in Tongling Region. Geological Publishing House, Beijing, pp. 1–131 (in Chinese).
Liu, X.B., 2002. Geological characteristics and ore-controlling factor analysis of Xinqiao S-Fe deposit. Express Inf. Mining Ind. 22, 13–15 (in Chinese).
Liu, Y.Q., 1991. Isotope Geochemical Research of Blanket Cu (-Fe-S) Deposit in Tongling Region. Geological Publishing House, Beijing, pp. 47–82 (in Chinese).
Loftus-Hills, G., Solomon, M., 1967. Cobalt, nickel and selenium in sulfides as indicators of ore genesis. Mineral. Deposita 2, 228–242.
Mao, J.W., Shao, Y.J., Xie, G.Q., Zhang, J.D., Chen, Y.C., 2009. Mineral deposit model for porphyry-skarn polymetallic copper deposits in Tongling ore dense district of Middle-Lower Yangtze Valley metallogenic belt. Mineral. Deposita 28 (2), 109–119 (in Chinese with English abstract).
Mao, J.W., Xie, G.Q., Duan, C., Franco, P., Dazio, I., Chen, Y.C., 2011. A tectono-genetic model for porphyry-skarn-stratabound Cu-Au-Fe and magnetite-apatite deposit along the Middle-Lower Yangtze River Valley, Eastern China. Ore Geol. Rev. 43 (1), 294–314.
Mao, J.W., Zhang, Z.H., Yu, J.J., Wang, Y.T., Niu, B.G., 2003. Geodynamic background of the large-scale metallogenic events in the Mesozoic in North China and adjacent regions: revelation from the precise ages of ore deposits. Sci. China Ser. D Earth Sci. 33 (4), 289–299 (in Chinese).
Maslennikov, V.V., Maslennikova, S.P., Large, R.R., Danyushevsky, L.V., 2009. Study of trace element zonation in vent chimneys from the Silurian Yaman-Kasay volcanic-hosted massive sulfide deposit (southern Urals, Russia) using laser ablation-inductively coupled plasma mass spectrometry (LA-ICPMS). Econ. Geol. 104, 1111–1141.
Mei, J.M., 2000. Chemical composition characteristic of pyrite in Zilingtou Au deposit, Suichang, Zhejiang Province, China. Geoscience 14 (1), 51–67 (in Chinese).
Meng, L.Y., 1994. Invasive type massive sulfide deposits in the Eastern China. Sci. China Ser. D Earth Sci. 24 (1), 76–80 (in Chinese).
Meng, L.Y., 1996. Stable isotopes compositions characteristics of invasive type massive sulfide deposits. Chin. Sci. Bull. 41 (9), 808–810 (in Chinese).
Morse, J.W., Luther, G.W., 1999. Chemical influences on trace metal-sulfide interactions in anoxic sediments. Geochim. Cosmochim. Acta 63, 3373–3378.
Pan, Y., Done, P., 1999. The lower Changjiang (Yangtzi/Yangtze River) metallogenic belt, east- center China: intrusion and wall rock hosted Cu-Fe-Au, Mo, Zn, Pb, Ag deposits. Ore Geol. Rev. 15 (4), 177–242.
Qi, J.Z., Liu, H.Y., Jiang, Y.H., 2000. Yanshanian subduction and strike-slipping regime of East China, and its control of ore localization. Miner. Res. 21 (4), 244–266 (in Chinese with English abstract).
Ravizza, G., Martin, C.E., German, C.R., Thompson, G., 1996. Os isotopes as tracers in seafloor hydrothermal system: metalliferous deposits from the TAG hydrothermal area, 26°N Mid-Atlantic Ridge. Earth Planet. Sci. Lett. 138, 105–119.
Raymond, O.L., 1996. Pyrite composition and ore genesis in the Prince Lyell copper deposit, Mt Lyell mineral field, western Tasmania, Australia. Ore Geol. Rev. 10, 231–250.

Reich, M., Becker, U., 2006. First-principles calculations of the thermodynamic mixing properties of arsenic incorporation into pyrite and marcasite. Chem. Geol. 225, 278–290.
Reich, M., Deditius, A., Chryssoulis, S., Li, J.W., Ma, C.Q., Parada, M.A., Barra, F., Mittermayr, F., 2013. Pyrite as a record of hydrothermal fluid evolution in a porphyry copper system: a SIMS/EMPA trace element study. Geochim. Cosmochim. Acta 104, 42–62.
Reich, M., Kesler, S.E., Utsunomiya, S., Palenik, C.S., Chryssoulis, S.L., Ewing, R.C., 2005. Solubility of gold in arsenian pyrite. Geochim. Cosmochim. Acta 69, 2781–2796.
Ren, Y.S., Liu, L.D., 2006. Hydrothermal colloidal pyrite in Tongling area, Anhui Province, and its metallogenic significance. Mineral. Deposita 25 (S), 95–98 (in Chinese with English abstract).
Rickard, D.T., 1970. The origin of framboids. Lithos 3 (3), 269–293.
Roberts, F.I., 1982. Trace element chemistry of pyrite: a useful guide to the occurrence of sulfide base metal mineralization. J. Geochem. Explor. 17, 49–62.
Sangster, D.F., 1990. Mississippi Valley-type and SEDEX lead-zinc deposits—a comparative examination. Institution of mining and metallurgy trans-actions, section B, Appl. Earth Sci. 99, 21–42.
Scott, S.D., 2008. Massive sulfide deposits on the deep ocean floor-the dawning of a new mining history. Pacific Rim: Mineral Endowment, Discovery & Exploration Frontiers. The Australasian Institute of Mining and Metallurgy, pp. 19–22.
Song, X.X., Zhang, J.K., 1986. Trace Element Characteristics of the Different Causes of Pyrite in China. Vol. 2. Collection of Institute of Mineral Resources, Chinese Academy of Geological Sciences, pp. 166–175 (in Chinese).
Sung, Y.H., Brugger, J., Ciobanu, C.L., Pring, A., Skinner, W., Nugus, M., 2009. Invisible gold in arsenian pyrite and arsenopyrite from a multistage Archaean gold deposit: Sunrise Dam Eastern Gold Fields Province, Western Australia. Mineral. Deposita 44, 765–791.
Tang, Y.C., Wu, Y.Z., Cu, G.Z., Xing, F.M., Wang, Y.M., Cao, F.Y., Chang, Y.F., 1998. Copper Gold Polymetallic Ore Deposit Geology in the Region Along Yangtze River in Anhui Province. Geological Publishing House, Beijing, pp. 1–351 (in Chinese).
Thomas, H.V., Large, R.R., Bull, S.W., Maslennikov, V., Berry, R.F., Fraser, R., Froud, S., Moye, R., 2011. Pyrite and pyrrhotite textures and composition in sediments, laminated quartz veins, and reefs at Bendigo gold mine, Australia: insights for ore genesis. Econ. Geol. 106, 1–31.
Tribovillard, N., Algeo, T.J., Lyons, T., Riboulleau, A., 2006. Trace metals as paleoredox and paleoproductivity proxies: an update. Chem. Geol. 232, 12–32.
Wang, S.W., Zhou, T.F., Yuan, F., Fan, Y., Zhang, L.J., Song, Y.L., 2015. Petrogenesis of Dongguashan skarn-porphyry Cu-Au deposit related intrusion in the Tongling district, eastern China: geochronological, mineralogical, geochemical and Hf isotopic evidence. Ore Geol. Rev. 64, 53–70.
Wang, Y., Zhu, X.K., Cheng, Y.B., 2013. Ore microscopy & Fe isotope of the Xinqiao deposit and their constraints on the ore genesis. J. Jilin Univ. Earth Sci. Ed. 43 (6), 1787–1798 (in Chinese with English abstract).
Wang, Y., Zhu, X.L., Mao, J.W., Li, Z.H., Cheng, Y.B., 2011. Iron isotope fractionation during skarn-type metallogeny: a case study of Xiao Cu-S-Fe-Au deposit in the Middle-Lower Yangtze Valley. Ore Geol. Rev. 43, 194–202.
Wang, Y.B., Liu, D.Y., Meng, Y.F., Zeng, P.S., Yang, Z.S., Tian, S.A., 2004a. SHRIMP U-Pb geochronology of the Xinqiao Cu-S-Fe-Au deposit in the Tongling ore district, Anhui, China. Geol. China 31 (2), 169–173 (in Chinese with English abstract).
Wang, Y.B., Tang, S.H., Wang, J.H., Zeng, P.S., Yang, Z.S., Meng, Y.F., Tian, S.H., 2004b. Rb-Sr dating the pyrite of the Xinqiao Cu-S-Fe-Au deposit, Tongling, Anhui Province. Geol. Rev. 50 (5), 538–541 (in Chinese with English abstract).
Wu, F.Y., Ge, W.C., Sun, D.Y., Guo, C.L., 2003. Discussions on the lithospheric thinning in Eastern China. Earth Sci. Front. 10 (3), 51–60 (in Chinese with English abstract).
Xiao, X., Zhou, T.F., Fan, Y., Xie, J., Zhang, L.J., 2016. LA-ICP-MS in situ trace elements and FE-SEM analysis of pyrite from the Xinqiao Cu-Au-S deposit in Tongling, Anhui and its constraints on the ore genesis. Acta Petrol. Sin. 32 (2), 369–376 (in Chinese with English abstract).
Xie, H.G., Wang, W.B., Li, W.D., 1995. The genesis and metallogenetic of Xinqiao Cu-S deposit, Anhui Province. Volcanol. Min. Res. 16 (2), 101–107 (in Chinese with English abstract).
Xie, J., 2012. Study on the Pyrite and the Implications for Genesis of Xinqiao Deposit, Anhui Province, China Master Thesis Hefei University of Technology, Hefei (in Chinese with English abstract).
Xie, J.C., Yang, X.Y., Du, J.G., Du, X.W., Xiao, Y.L., Qu, W.J., Sun, W.D., 2009. Re-Os precise dating of pyrite from the Xinqiao Cu-Au-Fe-S deposit in Tongling, Anhui and its implications for mineralization. Geol. Sci. 44 (1), 183–192 (in Chinese with English abstract).
Xie, Q.Q., Chen, T.H., Fan, Z.L., Xu, X.C., Zhou, Y.F., Shi, W.B., Xie, J.J., 2014. Morphological characteristics and genesis of colloform pyrite in Xinqiao Fe-S deposit, Tongling, Anhui Province. Sci. Sin. Terrae 44, 2665–2674 (in Chinese with English abstract).
Xu, G., Zhou, J., 2001. The Xinqiao Cu–S–Fe–Au deposit in the Tongling mineral district, China: synorogenetic remobilization of a stratiform sulfide deposit. Ore Geol. Rev. 18, 77–94.
Xu, K.Q., Zhu, J.C., 1978. Genesis discussion about sedimentary (or volcanic sedimentary) and reworked by hydrothermal copper deposits in several fault depression belts in Southeast China. Geol. Inform. Fujian 4, 1–110 (in Chinese).
Xu, W.Y., Yang, Z.S., Meng, Y.F., Zeng, P.S., Shi, D.N., Tian, S.H., Li, H.Y., 2004. Genetic model and dynamic migration of ore-forming fluids in Carboniferous exhalation-sedimentary massive sulfide deposits in Tongling District, Anhui Province. Mineral. Deposita 23 (3), 353–364 (in Chinese with English abstract).
Yang, B., Wang, Z.T., 1985. The new type ore body found and deposit genetic model in Tongguanshan Cu deposit. Mineral. Deposita 4 (4), 1–13 (in Chinese).
Yang, D.F., Fu, D.X., Wu, N.X., 1982. Genesis of pyrite type copper in Xinqiao and its neighboring region according to ore composition and structure. Issue of Nanjing Institute of Geology and Mineral Resources, Chinese Academy of Geological Sciences. Vol. 3 (4), pp. 59–68 (in Chinese with English abstract).
Yu, C.W., Cen, K., Bao, Z.Y., 1998. Dynamics of Mineralization. Geological Publishing House, Beijing, pp. 1–224 (in Chinese).
Zang, W.S., Wu, G.G., Zhang, D., Liu, A.H., 2004. Geological and geochemical characteristics and genetic analyses of Xinqiao Iron Orefield, Tongling. Geotecton. Metallog. 28 (2), 187–193 (in Chinese with English abstract).
Zhai, Y.S., Yao, S.Z., Lin, X.D., Jin, F.Q., Zhou, X.R., Wan, T.F., Zhou, Z.G., 1992. Metallogenic regularity of iron and copper deposits in the Middle-Lower valley of the Yangtze River. Mineral. Deposita 11 (1), 1–235 (in Chinese with English abstract).
Zhang, J., Deng, J., Chen, H.Y., Yang, L.Q., Cooke, D., Danyushevsky, L., Gong, Q.J., 2014. La-ICP-MS trace element analysis of pyrite from Chang'an gold deposit, Sanjiang Region, China: implication for ore-forming process. Gondwana Res. 26, 557–575.
Zhang, Y., 2015. Genesis of Xinqiao Cu-S-Fe Deposit, Tongling, Anhui Province, China Ph. D. Dissertation Central South University in Chinese.
Zhao, H.X., Frimmel, H.E., Jiang, S.Y., Dai, B.Z., 2011. LA-ICP-MS trace element analysis of pyrite from the Xiaoqinling gold district, China: implications for ore genesis. Ore Geol. Rev. 43, 142–153.
Zhou, T.F., Fan, Y., Yuan, F., 2008. Advances on petrogenesis and metallogeny study of the mineralization belt of the Middle and Lower Reaches of the Yangtze River area. Acta Petrol. Sin. 24 (8), 1665–1678 (in Chinese with English abstract).
Zhou, T.F., Zhang, L.J., Yuan, F., Fang, Y., Cooke, D.R., 2010. LA-ICP-MS in situ trace element analysis of pyrite from the Xinqiao Cu-Au-S deposit in Tongling, Anhui, and its constrains on the ore genesis. Earth Sci. Front. 17 (2), 306–319 (in Chinese with English abstract).